THE DESIGN AND ANALYSIS OF OPTICAL SCANNERS FOR OPTICAL

COHERENCE TOMOGRAPHY

By

Naresh Dhaubanjar

Presented to the Faculty of the Graduate School of

The University of Texas at Arlington in Partial Fulfillment

of the Requirements

for the Degree of

MASTER OF SCIENCE IN ELECTRICAL ENGINEERING

THE UNIVERSITY OF TEXAS AT ARLINGTON

AUGUST 2006

I dedicate this thesis to my father Badri Bhakta Dhaubanjar, my mother Subhadra Dhaubanjar, my brother Suresh Dhaubanjar, my sister Subarna K. Dhaubanjar and Jeena Dhaubanjar.

ACKNOWLEDGEMENTS

ABSTRACT

DESIGN AND ANALYSIS OF OPTICAL SCANNERS FOR OPTICAL

COHERENCE TOMOGRAPHY

Publication No. _____

Naresh Dhaubanjar, M. S.

The University of Texas at Arlington

Supervising Professor: Dr. Jung-Chih Chiao

A miniature fiber optic scanner capable of two-dimensional scanning for medical imaging is designed and developed. The scanner is actuated externally using an electromagnet. Nickel gel, a soft ferromagnetic material, is coated on the optical fiber. The performance of the scanner is characterized. Finite element analysis is performed to validate the theoretical and experimental results. A design and analysis of a cantilever type electrostatic zipping actuator and a bidirectional vertical thermal actuator are presented. The actuation principle, lumped modeling analysis, experimental results, and finite element analysis of both actuators are presented. The actuators are characterized statically and dynamically using an optical profiler. The design consideration in

displacement, electrostatic force, and electrostatic stability of the zipper actuator is presented. The zipper actuator is designed to withstand higher actuation voltages and a mechanical structure is implemented to avoid the electrical shortage of the device. The thermal actuator is optimized to obtain higher displacement required for the MEMS scanner. The scanners using these actuators can be designed to be mounted on a 3D OCT probe for *ex vivo* imaging.

TABLE OF CONTENTS

LIST OF ILLUSTRATIONS

LIST OF TABLES

CHAPTER 1

INTRODUCTION AND ACCOMPLISHMENTS

Optical coherence tomography requires optical scanners for the imaging of biological tissues and organs. Various configurations of 1D and 2D scanners have been developed in the past. Similarly, various actuation mechanisms have been implemented to actuate the scanning mirror, such as electromagnetic, thermal, electrostatic and piezoelectric. In this thesis, 1D and 2D optical scanners have been investigated, and electromagnetic, electrostatic, and thermal actuation mechanism has been implemented to design the optical scanners.

A miniature fiber optic scanner capable of two-dimensional scanning for medical imaging has been developed. The scanner is actuated externally using an electromagnet. It can be used in an optical coherence tomography for *in vivo* imaging of tissues and organs. Ferromagnetic material, nickel, is used for the actuation mechanism which is mixed with enamel paint and is coated on the optical fiber. The ferromagnetic material is first characterized in terms of magnetic property which is then used to characterize the performance of the scanner. Finite element analysis is performed to validate the theoretical and experimental results. The performance of the scanner depends on the length of the fiber under actuation and the thickness of the ferromagnetic gel. The length and thickness are selected to obtain the optimum

performance of the scanner. The results showed a 0.8-mm linear displacement under the influence of a static magnetic field of 17.6 KA/m in a fiber with a moveable length of 4.2cm. Dynamic analysis showed linear displacement of 0.83mm with an input current amplitude of 41mA and a magnetic field of 2.4 KA/m.

A cantilever type electrostatic zipping actuator and a bidirectional vertical thermal actuator that can be used to design 2-D optical scanner are presented. The scanners using these actuators can be designed to be mounted on the 3D OCT probe which can be used for *ex vivo* imaging. The actuation principle of a zipper actuator is based on the electrostatic force between the curved cantilever and the bottom electrode that pulls the cantilever down. The 3-D imaging is made possible by implementing four such zipper actuators. The vertical displacements of different devices configurations were found ranging from 26 μm to 450 μm while the actuation voltages varied in the range of 12 V to 45.3 V for complete actuation. The actuation principle of a thermal actuator is based on the asymmetrical thermal expansion of pseudo-bimorph microstructures due to the difference in electrical resistance of two stacked poly-silicon layers. The design consideration in displacement, electrostatic force, and electrostatic stability of the zipper actuator is presented. The thermal actuator is optimized to obtain higher displacement required for the MEMS scanner. The actuators are characterized statically and dynamically using the optical profiler. Finite element analysis is performed to validate the theoretical and experimental results. The maximum displacement of thermal actuator was found to be 10.881 μm at an input voltage of 7 V.

CHAPTER 2

OPTICAL COHERENCE TOMOGRAPHY

The principle medical imaging systems found in today's medical facilities include X-ray imaging, magnetic resonance imaging, endoscope imaging, and ultrasound imaging. Extensive research has been done for the improvement of these imaging systems. Optical coherence tomography (OCT) has emerged in recent years since its potentials in medical applications. It was first demonstrated in 1991 with approximately 30μm axial resolution [1]. It is particularly suitable for ophthalmic applications and other tissue imaging that requires micrometer resolutions and millimeter penetration [2]. These are critical advantages over other imaging systems. OCT can perform high resolution, cross-sectional tomographic imaging of biological tissues and internal organs by measuring backscattered light. The principle of OCT is analogous to the ultrasound imaging where OCT uses light instead of sound for realizing imaging. The images obtained from OCT are of micron-level resolution.

The main drawback of OCT is the imaging speeds. Conventional OCT relies on two dimensional scanning mechanisms to acquire the image, i.e. an axial depth scan that samples the light returning from different depth and a lateral scan that samples the light returning from lateral dimensions. The speeds of these OCT depend on the speeds of these axial and lateral scan. This chapter discusses a brief overview of optical coherence

tomography, current research on OCT, and currently available 1D and 2D scanner for 2D and 3D imaging respectively.

2.1 Brief Overview of Optical Coherence Tomography

The origin of OCT lies in the early work on white light interferometry. The development of optical coherence-domain reflectometry (OCDR) was followed by the white light interferometry. OCDR is a one dimensional optical ranging technique which uses short coherence length light and interferometric detection technique for high sensitivity and high resolution range information [3]. The application of OCDR was then realized in ranging measurements of eye structures within a precision of 0.03 mm [4]. OCT, an extended technique of the OCDR, was then developed for the tomographic imaging of biological tissues. Today, OCT has become a simple, low cost and noninvasive tool for medical imaging [5-7].

Fig. 2.1 shows the basic OCT system configuration. The system is based on a fiber-optic Michelson interferometer. A broadband light source is split by a fiber-optic
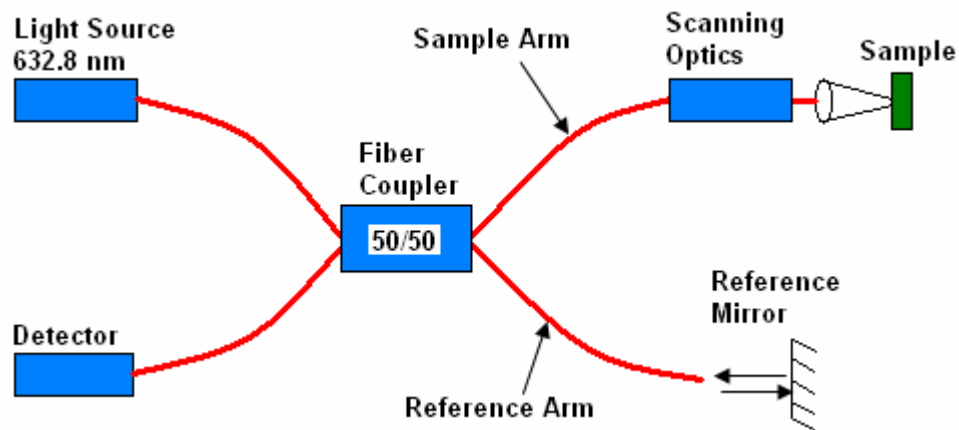
Figure 2.1: Optical coherence tomography system configuration.

4

50/50 coupler and sent to the sample and reference arms. The light exiting from the sample arm is focused onto the sample using an appropriate scanner. The reflected light is collected back into the fiber. The light exiting from reference arm is directed at the reference mirror. The reflected light from the reference mirror is collected back into the fiber. The light from the sample arm and reference arm is then combined at the detector. The detector measures the intensity of the output optical beam. Interference occurs at the detector only when the distance of the reflection from the sample is matched to the length of the reference arm within the coherence length of the source. A scan of the sample is then performed by scanning the reference mirror position and simultaneously recording the interferometric signal. The electrical signal obtained from the detector is then amplified, band-pass filtered, demodulated, and stored with a digital form.

2.2 Current Research on Optical Coherence Tomography

Optical coherence tomography is a very young imaging technology compared to the rest of the imaging tools such as X-ray imaging, magnetic resonance imaging, endoscope imaging, and ultrasound imaging. Extensive research has been going on to identify the role of OCT in medical fields. OCT has been used extensively in ophthalmology where it can detect and diagnose early stages of disease before irreversible loss of vision occurs. It has been used as non-invasive, non-contact imaging of the anterior of the eye and retina [8, 9] helping with the diagnosis of various macular disease and glaucoma, and for the management of acute retinopathy of prematurity [10], OCT is also used to detect the early neoplastic change which is an early stage of cancer. Extensive research has been done to use OCT for the diagnosis of early neoplasia in

gastrointestinal [11], pulmonary [12], and biliary tracts [13]. It has been used as microsurgical intervention on vessels and nerves [14].

Research is being conducted to improve the imaging performance for higher axial resolution, sensitivity and speed. The light source needs to have a broad emission spectrum for high axial resolution. Therefore broadband light sources such as ultra-short pulsed lasers and white light sources are under investigation [2, 15, 16]. The maximum penetration depth of the imaging system depends upon illumination power but is inversely proportional to the imaging speed. Improvement of OCT in terms of scanning speeds is also under investigation [17, 18].

2.3 Typical Optical Scanner

Optical scanners may operate in a high speed scanning mode or static beam steering mode. For high speed scanning, device operates in its natural frequencies. In the beam steering mode, a series of single axis mirrors may be employed. A simplest design found in literature is a single beam design shown in Fig. 2.2 (a). It consists of a mirror fixed at the end of a mechanical beam. The bending and torsion of the beam produces two transverse rotations of the mirror generating two scanning modes [19]. The main disadvantage of this design is that the bending and torsion produces not only transverse but also translation which can alter the alignment of the light beam.

Most of the mirror design found in the literature employs electrostatic actuation scheme, as shown in Fig. 2.2 (b) and (c) [20-22]. These scanners provide better decoupling between two scanning modes. For better ranges of motion necessary for use in optical coherence tomography, the gap between the mirror and the electrostatic pads

6

would have to be large which consequently requires very high operating voltages. The

main disadvantage of this actuation mechanism is that they are very complex.
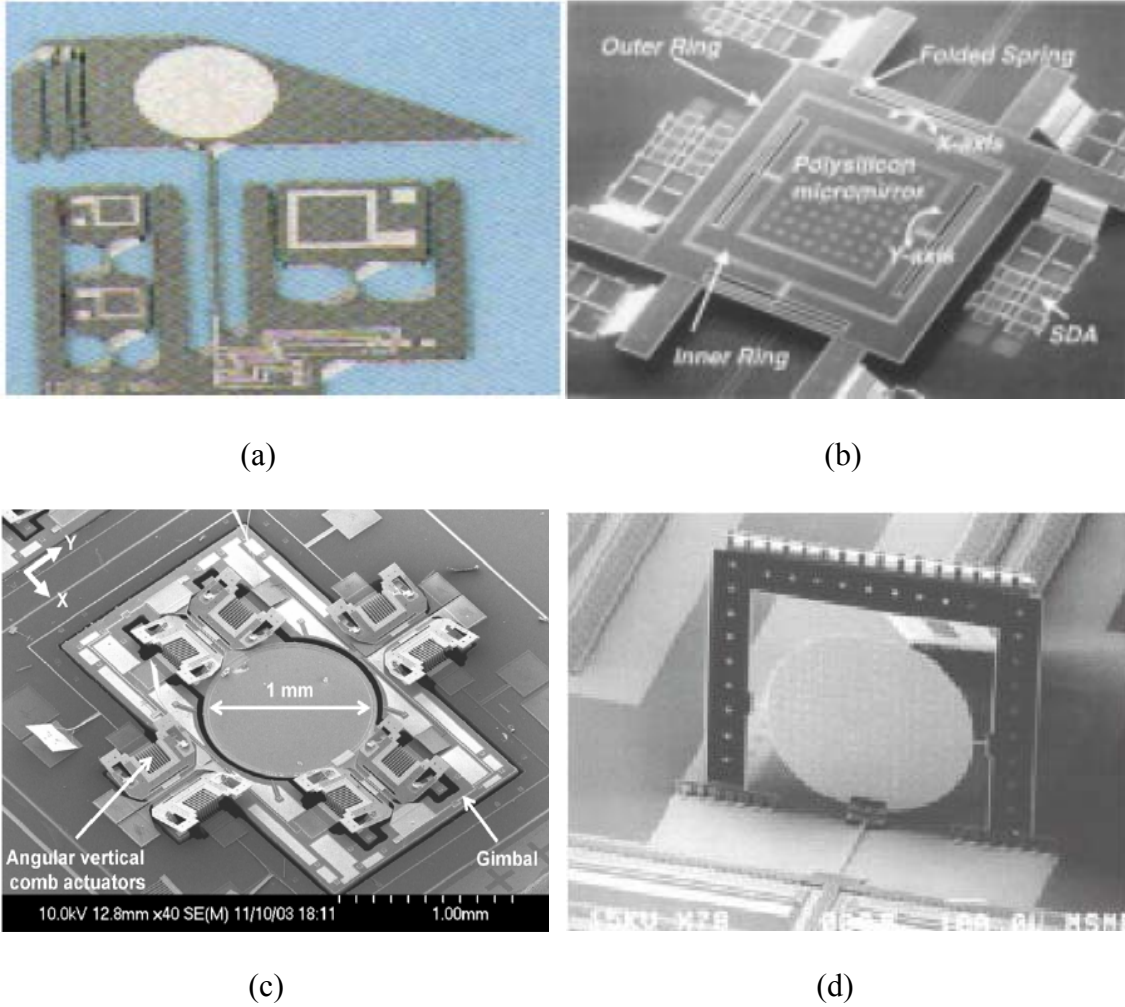
Figure 2.2: Typical optical scanner: (a) single beam design, (b) double gimbals, (c) angular vertical comb, (d) 3D self-assembly.

Some designs found in literature employs a 3D self-assembly structure [23, 24]. The fabrication and assembly of this design is a complex process and the packaging is a relatively complex task.

7

2.4 Scope of This Thesis

A design of an optical fiber based one directional scanner is presented. The optical fiber based scanner is small in size and offers low cost. Since the device itself has non-electrical control, the power consumption is very low. Similarly, the MEMS based zipper actuator and thermal actuator operates at low voltage and provides higher displacement. The optical fiber based scanner and zipper actuator based 2D scanner can be used for *in vivo* imaging, and thermal actuator based 2D scanner can be used for *ex vivo* imaging.

CHAPTER 3

OPTICAL FIBER BASED 1-D SCANNER

<u>3.1 Introduction</u>

Fiber optical devices are under intensive development these days in the field of optical measurement instruments, and medical imaging. The compactness of the optical devices makes it suitable for the applications where size, precision and low power consumption is critical. Fiber optical devices have been used in the fields of telecommunications such as fiber optical switches, and optical amplitude modulator [25-27], medical imaging [28], and sensors [29-32]. Fiber optical devices have been developed with piezoelectric [33], electrostatic [34, 35], thermal [36, 37], and electromagnetic [38-40] actuation. Among these, piezoelectric and electrostatic devices require high voltage input which may not be suitable for *in vivo* applications, and thermal devices have higher power consumption. Optical devices using electromagnetic actuation, on the other hand, provide higher force, large deflection, and low power consumption. Therefore, considering the size, precision, force, speed and low power consumption, devices with electromagnetic actuation provides better performance.

In this chapter, a fiber optic scanner using external magnetic actuation for medical imaging has been developed. It is capable of two dimensional scanning and it can be used in an optical coherence tomography for *in vivo* and *in vitro* imaging of

tissues and organs. The magnetic actuation is achieved using a soft ferromagnetic material. The ferromagnetic material mixed with enamel paint and is coated on an optical fiber. The ferromagnetic material was first characterized in terms of magnetic properties. The static and dynamic characterization of the scanner was performed. The theoretical and experimental results were verified using the finite element analysis. The general description of the optical scanner is introduced in the section 3.2. Section 3.3, 3.4 and 3.5 address the theory and physical principle behind the magnetic actuation, experimental results, and finite element analysis respectively.

<p style="text-align:center;">3.2 General Description of Optical Fiber Based 2-D Scanner</p>

Figure 3.1 shows the configuration of the optical fiber based 2-D scanner demonstration. It consists of an external electromagnet, a single-mode optical fiber coated with nickel powder, a HeNe laser, objective lens, and a position sensitive detector (PSD).
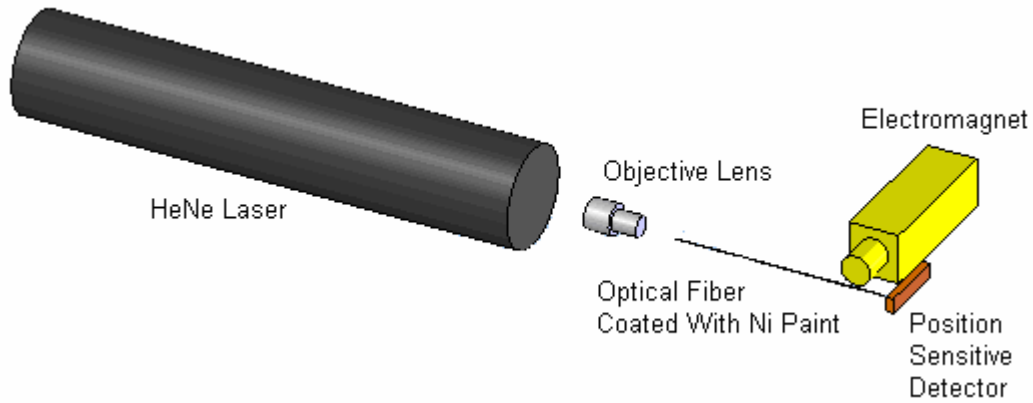
Figure 3.1: Demonstration configuration of the fiber optic scanner.

The HeNe laser is used as a light source with a wavelength of 632.8 nm and an optical power of 20mW. Light is coupled using the direct butt coupling method with a collimated lens. The focal length of objective lens is 0.5 mm.

The position sensitive detector consists of an active area, a uniform resistive layer, and a pair of electrodes formed on both ends of the resistive layer for extracting position signals [41]. The active area has a PN junction that generates photocurrent by means of photovoltaic effect. Figure 3.2 shows a sectional view of a PSD.
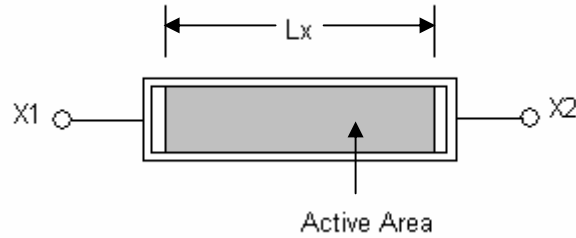
Figure 3.2: Sectional view of a PSD.

When a spot light strikes the PSD, an electric charge proportional to the light intensity is generated at the incident position which is driven through the resistive layer and collected by the output electrodes X_1 and X_2 as photocurrents. The incident light position can be calculated by the following relationship.

$$\frac{I_{X_1}}{I_{X_2}} = \frac{L_X - X}{X} \qquad (3.3.1)$$

I_{X_1} = Output current from the electrode X_1,

I_{X_2} = Output current from the electrode X_2,

11

L_X = Length of the active area,

X = Distance from the electrode X1 to the light input position.

The electromagnet with a resistance of 30 Ω is used as the magnetic field generator. The strength of magnetic fields with a 3, 4 and 5 mm distance away from the core were measured by F. W. Bell 5080 Gaussmeter. The results will be discussed in the section 3.4.2.

When this scanner is implemented in the imaging system, the light exiting from the optical fiber is focused into the sample. The light reflected from the sample is collected back into the fiber which is combined with the reflected light from reference mirror, and the scanning is performed as described in section 2.1.

3.3 Theory and Physical Principle

Researchers have used permanent magnetic materials such as NdFeB and CoPt for their high permeability, low coercivity, low hysteresis loss, versatility in functions, high strength of magnetic moments, and easiness in implementation [42, 43]. Low coercivity is an important material property for low power and fast speed applications because the magnetic remnant flux can be removed with low reversed magnetic field. The advantage of pre-magnetic poling NiFe permalloy and permanent magnet is that the device can be actuated externally without using any wire, and they have zero power consumption. These advantages can provide solutions to the applications which require low power consumption and minimum dimension. The theory and physical principle behind the magnetic actuation of the fiber are described in this chapter. These subjects

12

will be discussed in the order of mechanical analysis, magnetic analysis, and static displacement, and resonant frequency.

3.3.1 Mechanical Analysis

When the optical fiber coated with the nickel-based ferromagnetic gel is subjected to a magnetic force, the longitudinal axis of the optical fiber deviates from its original position because of the bending of the fiber. This deviation at any cross section of the optical fiber is called the deflection at that section. The transverse shear i.e. the sliding of a cross section relative to the adjacent cross section also plays role on the bending but it is chosen to be neglected in our analysis because the cross section of the optical fiber is negligible in comparison to the length of the fiber [44].

It is important to know the moment-curvature relationship in order to perform the mechanical analysis for the bending of fiber. If we select X-Y axis as in Fig. 3.3 (a) and take sign convention for bending moment as in Fig. 3.3 (b), the moment-curvature relationship is given by the Eq 3.3.2,

$$M = E \, I \, \frac{d^2 v}{dx^2} \qquad\qquad (3.3.2)$$

M = Bending Moment

E = Young's Modulus

$I = \dfrac{\pi \, r^4}{4} = $ Circular Area Moment of Inertia

v = Displacement in the y Directon

r = Radius of the Optical Fiber

13

(a)   (b)
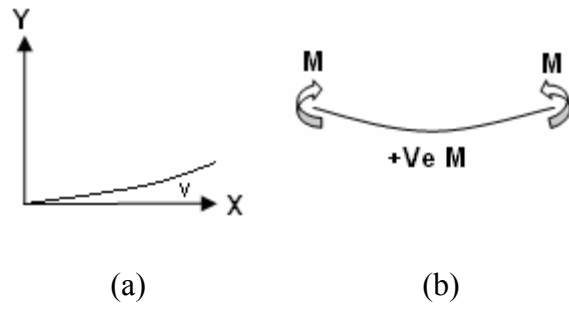
Figure 3.3: Sign convention, (a) Positive X-Y axis (b) Positive bending moment.

For the optical fiber without ferromagnetic gel coating, the loading is shown in Fig. 3.4.
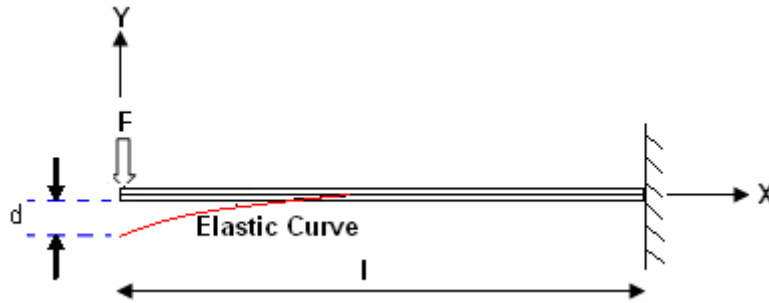
Figure 3.4: Loading on an optical fiber.

Taking the positive bending moment as shown in Fig. 3.3, the bending moment at distance x is given by

$$M = -F_{sp} * x \tag{3.3.3}$$

Where F_{sp} is spring force.

Substituting Eq. 3.3.2,

14

$$E \, I \, \frac{d^2v}{dx^2} = -F_{sp} * x \tag{3.3.4}$$

Integrating Eq. 3.3.4,

$$\int E \, I \, \frac{d^2v}{dx^2} = \int - F_{sp} * x$$

$$E \, I \, \frac{dv}{dx} = - \frac{F_{sp} \, x^2}{2} + C_1$$

At $x = l$, the bending slope is equal to zero,

$$C_1 = \frac{F_{sp} \, l^2}{2}$$

$$E \, I \, \frac{dv}{dx} = - \frac{F_{sp} \, x^2}{2} + \frac{F_{sp} \, l^2}{2} \tag{3.3.5}$$

Integrating Eq. 3.3.5

$$\int E \, I \, \frac{dv}{dx} = \int \left(- \frac{F_{sp} \, x^2}{2} + \frac{F_{sp} \, l^2}{2} \right)$$

$$E \, I \, v = - \frac{F_{sp} \, x^3}{6} + \frac{F_{sp} \, l \, x}{2} + C_2$$

At $x = l$, the displacement in the y direction is zero,

$$C_2 = - \frac{F_{sp} \, l^3}{3}$$

$$E \, I \, v = - \frac{F_{sp} \, x^3}{6} + \frac{F_{sp} \, l^2 \, x}{2} - \frac{F_{sp} \, l^3}{3} \tag{3.3.6}$$

From Eq. 3.3.5, the bending slope of the fiber at x = 0 is given by

$$S = \frac{dv}{dx} = \frac{F_{sp}\,l^2}{2EI} \qquad (3.3.7)$$

Similarly, from Eq. 3.3.6, the deflection of the optical fiber at x = 0 is

$$v = -\frac{F_{sp}\,l^3}{3EI} \qquad (3.3.8)$$

The negative sign of the deflection indicates that the deflection of fiber is downward. The magnitude of the deflection can be written as

$$v = \frac{F_{sp}\,l^3}{3EI} \qquad (3.3.9)$$

Where F_{sp} is the spring restoring force that counteracts the magnetic force generated due to magnetic fields, v is the linear displacement of the fiber, and l is the length of the optical fiber under the bending action.

Eq. 3.3.9 can be rearranged as

$$F_{sp} = \frac{3EI}{l^3} v$$

$$F_{sp} = K'v \qquad (3.3.10)$$

In Eq. 3.3.10, K' is the linear spring constant.
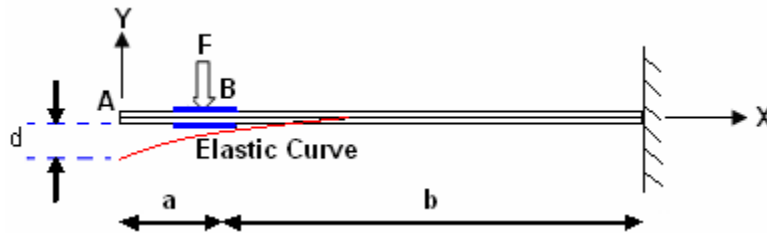
Figure 3.5: Loading on optical fiber with ferromagnetic gel.

For the optical fiber with the ferromagnetic gel coating, the loading is shown in Fig. 3.5. The total deflection of the optical fiber, d, is equal to the sum of deflection of fiber at the point B due to magnetic force and the slope of the fiber from B to A multiplied by the distance between the point B and the tip A. Using Eq. 3.3.7 and 3.3.9, total linear deflection, d, is given by

$$d = \frac{F_{sp} b^3}{3EI} + \frac{F_{sp} a^2}{2EI} a \qquad (3.3.11)$$

The spring restoring force and linear spring constant can be obtained by rearranging the Eq. 3.3.11,

$$F_{sp} = \frac{1}{\left(\dfrac{b^3}{3EI} + \dfrac{a^3}{2EI} \right)} d = K d \qquad (3.3.12)$$

3.3.2 Magnetic Analysis

All ferromagnetic materials contain microscopic regions called domains, within which all magnetic moments are aligned. The boundaries between various domains having different orientations are called domain walls. In an unmagnetized sample, the domains are randomly oriented so that the net magnetic moment is zero. When the sample is placed in an external magnetic field, the magnetic moments of domains tend to align with the magnetic field resulting in a magnetized sample. If the magnetic field is applied for long time, the sample becomes saturated. The saturation of the sample depends upon the material, and the volume of the sample.

Fig. 3.6 illustrates this phenomenon. In Fig. 3.6 (a), the external magnetic field is zero as the domains are randomly oriented. When an external magnetic field is

17
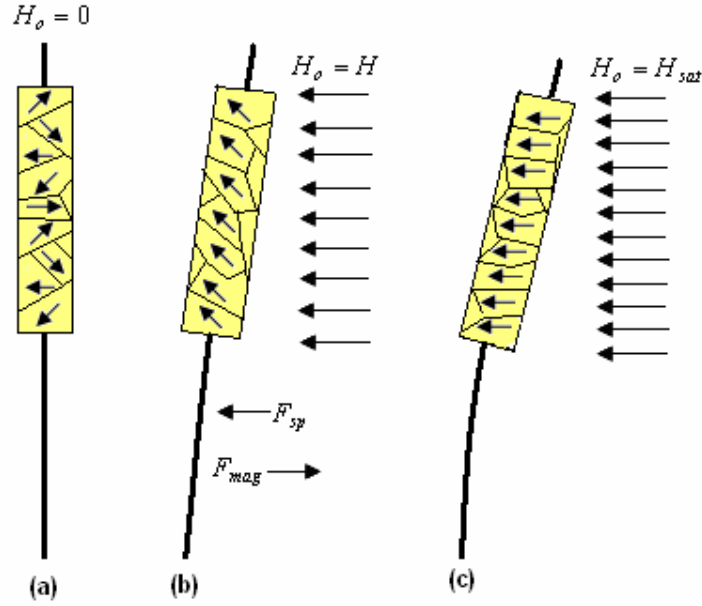
Figure 3.6: Principle of ferromagnetic actuation with (a) H_o=0, (b) H_o=H, and (c) H_o=H_{sat}

applied, the domains starts to align with the magnetic field and the nickel based ferromagnetic gel starts to get magnetized. As a result, there exists an attraction force between the gel and the applied magnetic field, and therefore the optical fiber starts to bend, as shown in Fig. 3.6 (b). Maximum displacement of the optical fiber is achieved when all the domains are aligned with the applied magnetic field, i.e. the gel becomes saturated, Fig. 3.6 (c).

Let us consider an isolated small cylindrical volume of magnetically polarized nickel-based ferromagnetic gel with a geometric axis aligned with the magnetization vector M, as shown in Fig. 3.7 [45]. The cylinder has a length of d and a cross section of a_d.
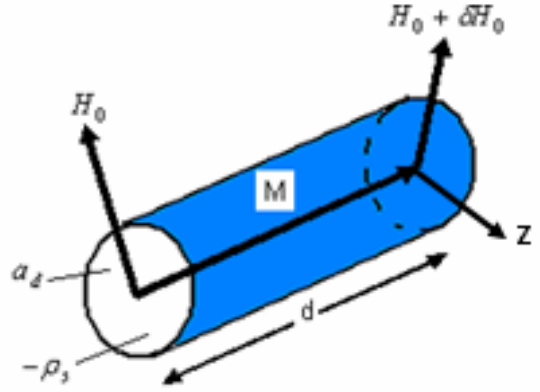
Figure 3.7: Analysis of induced magnetic force.

When the magnetic field H_0 is applied to this cylindrical volume, poles of density $\rho_s = \mu_0 M$ appear in equal number but of opposite polarity on the ends of area a_d.

$$\text{Volume of ferromagnetic gel} = \delta V = a_d\, d$$

The force experienced by the above volume is given by the Eq. 3.3.13.

$$-H_0\, \rho_s\, a_d + (H_0 + \delta H_0)\rho_s\, a_d = \delta H_0\, \rho_s\, a_d \qquad (3.3.13)$$

In Eq. 3.3.13, δH_0 is the change in magnetic field along the direction of d. Therefore,

$$\delta H_0 = (d \bullet \nabla)H_0 = \left(\frac{d}{M}\right)(M \bullet \nabla)H_0$$

And the magnetic force density is

$$\text{Force density} = \mu_0 (M \bullet \nabla)H_0 \qquad (3.3.14)$$

In Eq. 3.3.14, $\mu_0 M$ is the vector moment per unit volume because dipole moment m is given by

$$m = \mu_0\, M\, a_d\, d$$

For soft magnetic material, total magnetic force is

$$F_{mag} = (m \bullet \nabla)H_0$$
$$F_{mag} = \mu_0 \cdot M \cdot V \cdot \nabla H_0$$

$$F_{mag} = \mu_0 \cdot M \cdot V \cdot \left(\frac{dH_0}{dx} + \frac{dH_0}{dy} + \frac{dH_0}{dz} \right) \qquad (3.3.15)$$

The magnetic field is highest at the z-direction in our system configuration. Therefore, for a rough estimation of the magnetic force, the gradient of magnetic field at the x and y-direction is neglected. Hence,

$$F_{mag} = \mu_0 \cdot M \cdot V \cdot \frac{dH_0}{dz} \qquad (3.3.15)$$

3.3.3 Static Displacement

In the section 3.3.2 and 3.3.3, the magnetic force and the spring restoring force have been formulated. For the fiber to remain in a particular position when actuated by an electromagnet, the spring restoring force and the magnetic force should be at equilibrium. Mathematically,

$$F_{sp} = F_{mag}$$

$$\frac{1}{\left(\dfrac{b^3}{3EI} + \dfrac{a^3}{2EI} \right)} d = \mu_0 \cdot M \cdot V \cdot \frac{dH_0}{dz}$$

$$d = \mu_0 \cdot M \cdot V \cdot \frac{dH_0}{dz}\left(\frac{b^3}{3EI} + \frac{a^3}{2EI}\right) \tag{3.3.16}$$

3.3.4 Resonant Frequency

At the resonant frequency of operation, the scanner requires minimal power, the optical fiber experiences maximum displacement, and the oscillating motion of the optical fiber is pure sinusoidal. The resonant frequency of the scanner can be obtained using the Rayleigh's method [46]. Let us consider an optical fiber curve carrying a concentrated mass M_g of ferromagnetic gel as shown in Fig. 3.8. In the figure, m_f is the mass of the optical fiber.
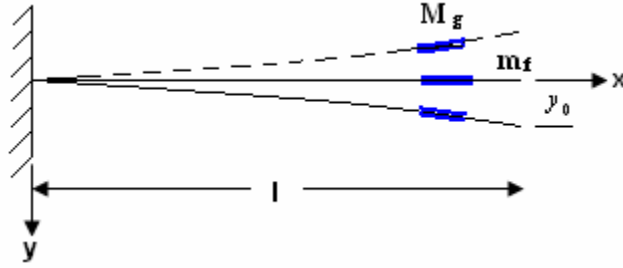
Figure 3.8: Quarter cosine wave as a Rayleigh shape of an optical fiber.

The system is assumed to be horizontal at x = 0 and has no curvature or bending moment at the end of the length of fiber *l*. A quarter cosine wave of the fiber is given by

$$y = y_0\left(1 - Cos\frac{\pi x}{2l}\right) \tag{3.3.17}$$

Further, consider a bending moment M acting on an element dx of the fiber as shown in Fig. 3.9.

21
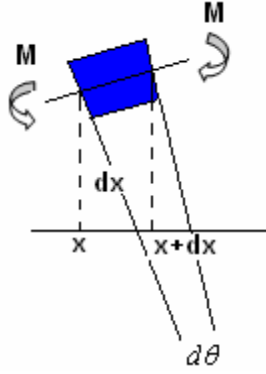
Figure 3.9: An element in the optical fiber.

The element is originally straight and is bent with an angle $d\theta$ due to the bending moment. The work done by bending moment M is given by

$$W = \frac{1}{2} M \, d\theta \qquad (3.3.18)$$

The factor $\frac{1}{2}$ appears in the Eq. 3.3.18 because both M and $d\theta$ are increasing from zero together. This work done is stored as potential energy in the beam element. If the slope at the fixed end is $\frac{dy}{dx}$, the slope at the free end is $\frac{dy}{dx} + \frac{d^2 y}{dx^2} dx$. Therefore $d\theta$ is the difference between the slope at the free end and the slope at the fixed end which is given by

$$d\theta = \frac{d^2 y}{dx^2} dx \qquad (3.3.19)$$

$$d \, P.E. = \frac{1}{2} M \frac{d^2 y}{dx^2} dx \qquad (3.3.20)$$

where P.E. is the potential energy.

Substituting the expression of M from Eq. 3.3.2 to Eq. 3.3.20,

22

$$d\,P.E. = \frac{1}{2}E\,I\left(\frac{d^2y}{dx^2}\right)^2 dx \qquad (3.3.21)$$

The total potential energy of the fiber can be obtained by integrating Eq. 3.3.21 over the length l.

$$P.E. = \int_0^l d\,P.E. = \frac{1}{2}E\,I\int_0^l\left(\frac{d^2y}{dx^2}\right)^2 dx \qquad (3.3.22)$$

The total kinetic energy of the fiber is the sum of kinetic energies of such elements and is given by

$$\frac{1}{2}m_f\,v^2 = \frac{1}{2}(\mu_1\,dx)(y\,\omega)^2$$

$$K.E. = \frac{1}{2}\mu_1\,\omega^2\int_0^l y^2\,dx \qquad (3.3.23)$$

where, μ_1 is the mass per unit length of the optical fiber and ω is the resonant frequency. Substituting the expression of y from Eq. 3.3.17 to 3.3.22 and 3.3.23 and integrating, we obtain

$$P.E. = \frac{\pi^4}{64}\frac{E\,I}{l^3}y_0^{\,2} \qquad (3.3.24)$$

$$K.E. = \mu_1\,\omega^2\,y_0^{\,2}\,l\left(\frac{3}{4}-\frac{2}{\pi}\right) \qquad (3.3.25)$$

The potential energy of the system is not affected by the addition of the mass of ferromagnetic gel. However, the kinetic energy of the system is increased by $\frac{1}{2}M_g\,\omega^2\,y_0^{\,2}$. Therefore the total kinetic energy of the system is given by the Eq. 3.3.26:

$$K.E. = \mu_1 \omega^2 y_0^2 l \left(\frac{3}{4} - \frac{2}{\pi} \right) + \tfrac{1}{2} M_g \omega^2 y_0^2$$

Since, $m_f = \mu_1 l,$

$$K.E. = \frac{1}{2} \omega^2 y_0^2 \left[M_g + m_f \left(\frac{3}{2} - \frac{4}{\pi} \right) \right] = \frac{1}{2} \omega^2 y_0^2 \left(M_g + 0.23 m_f \right) \quad (3.3.26)$$

According to the Rayleigh's method, the potential energy and the kinetic energy are equated and solved for ω to obtain resonant frequency.

$$\frac{1}{2} \omega^2 y_0^2 \left(M_g + 0.23 m_f \right) = \frac{\pi^4}{64} \frac{EI}{l^3} y_0^2$$

$$\omega^2 = \frac{3EI}{l^3 \left(M_g + 0.23 m_f \right)}$$

$$f = \frac{1}{2\pi} \sqrt{\frac{3EI}{l^3 \left(M_g + 0.23 m_f \right)}} \qquad (3.3.27)$$

3.4 Experimental Results

3.4.1 Fabrication

Electroplating, thermal evaporation, and electron beam evaporation has been used to coat magnetic thin films on the magnetic devices. Yun-Ho Jang *et al.* used electroplating to deposit thin film of nickel on out-of-plane micromirror [47]. Mitsunori Saito *et al.* used dip-coating technique to coat black paint on the fiber to protect the fiber from visible and UV light [48]. Yoko Okano *et al.* deposited magnetic films on the micromirror by magnetron sputtering [49]. Sol-gel method has also been used to coat thin films on the magnetic devices [50]. The quality of thin films obtained from

electroplating, magnetron sputtering, thermal evaporation, and electron beam evaporation depends on fabrication temperature, pressure, current and voltage.
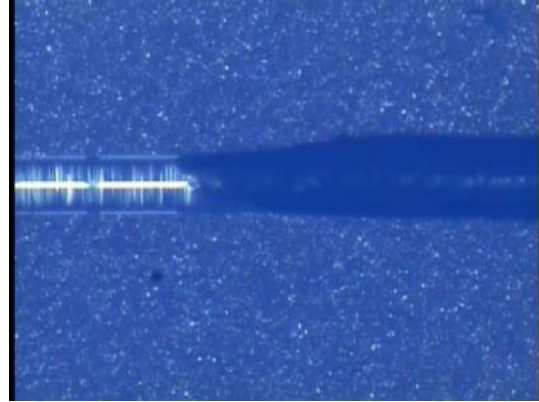
(a)   (b)
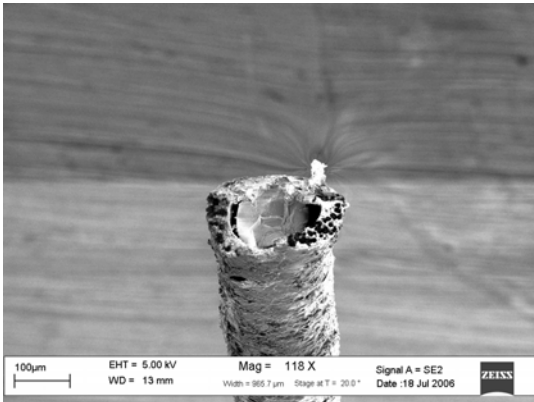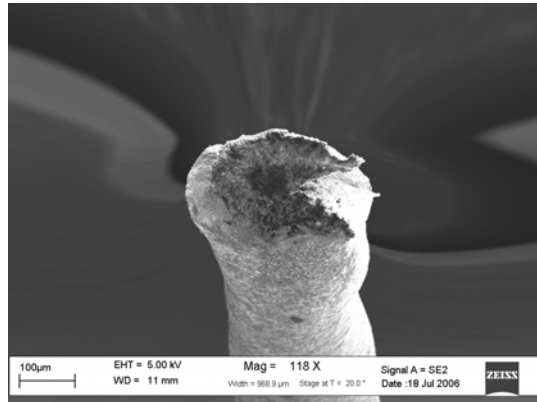
(c)   (d)

Figure 3.10: Microscopic and SEM images for (a), and (c) 2-layer coating, and (b), and (d) 3-layer coating.

In this work, nickel based ferromagnetic gel has been coated on the fiber using the technique similar to [51], where the nickel powder is homogenously mixed with enamel paint, and then it is brush coated on the fiber. A single mode optical fiber is left

to soak in dichloromethane solution for 15 minutes to remove the acrylic coating and then washed in acetone. 30% nickel powder by weight is mixed with 70% enamel paint by weight in a plastic plate. It is mixed uniformly using paint brush. Thus obtained gel is painted approximately 5 mm below the tip of the fiber. The coated fiber is then left to dry for 20 minutes. Multiple coating can be applied after the first coating is dry. The brush coating can be done multiple times in order to get desired thickness. The thickness of a single coating is approximately 15-20 μm. Experiment was carried out on the fibers that are coated twice and three times. The thickness of twice coated gel is approximately 30-40 μm and thickness of gel is approximately 50-60 μm when coated three times. Fig. 3.10 (a), (b), (c), and (d) shows the microscopic and scanning electron microscope (SEM) photo of the optical fiber coated two and three times using. The thicknesses are approximately 40 and 60 μm respectively.

3.4.2 Magnetization vector and Gradient of Magnetic Field Measurement

The fiber optic scanner has been characterized to ensure that its behavior is accurately predicted by the theory and physical principle. In contrary to pre-poled ferromagnetic materials which give rise to magnetic torques under the influence of external magnetic field, non-poling ferromagnetic materials such as nickel are attracted to external magnetic fields. This phenomenon can be implemented to obtain the static and dynamic results of the fiber optic scanner.

A thin film of magnetic gel with 30% of nickel powder by weight and 70% of enamel paint by weight is homogenously mixed to determine the magnetic hysteresis curve of the ferromagnetic gel using a MicroMag™ Alternating Gradient Magnetometer

26

Model 2900 (Princeton Measurement Corporation, Princeton, NJ). The prepared sample is a planar film of 3.55 mm by 5.4 mm in area and 0.13 mm thick. Fig. 3.11 shows the several key parameters such as coercivity field H_c, remnant flux M_r, and saturation flux M_s. This measurement were taken with the sample in parallel with the external magnetic field in order to minimize the demagnetization effect. The saturation magnetic volume density of the magnetic gel was found to be 86.7 KA/m.
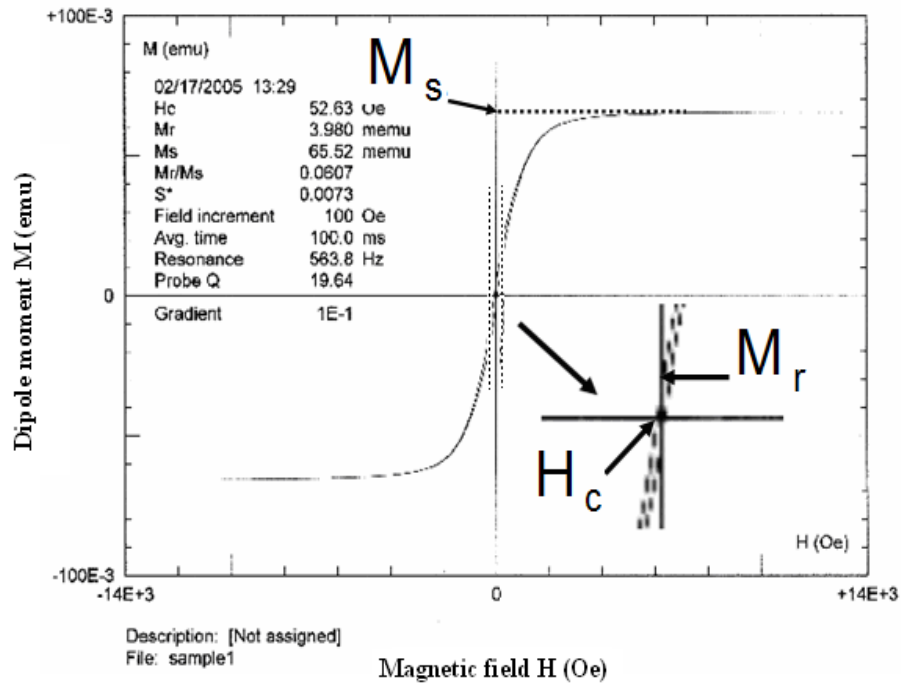
Figure 3.11: The dipole moment-magnetic field (m-H) curve of the nickel powder based magnetic gel [52].

The general expression for the magnetization vector M is obtained by analyzing the measurement taken from MicroMag. The data thus obtained is converted to the appropriate unit. The quadratic equation of the magnetization vector is obtained by first

27

plotting the magnetic field and magnetization vector. The curve fitting method is then implemented in order to obtain the quadratic equation that accurately predicts the magnetization vector with respect to the applied magnetic field. The magnetic field and dipole moment measured from MicroMag is tabulated in table 3.1.

Table 3.1: Magnetic field and dipole moment using MicroMag

Volume of sample $= 2.4921$ mm^3

H (Oe)	m (emu)
$9.82*10^1$	$1.03*10^{-2}$
$1.98*10^2$	$1.58*10^{-2}$
$2.98*10^2$	$2.07*10^{-2}$
$3.98*10^2$	$2.51*10^{-2}$
$4.97*10^2$	$2.91*10^{-2}$
$5.97*10^2$	$3.28*10^{-2}$

The quadratic equation is shown in Fig. 3.12 and Eq. 3.4.1.

$$y = -4.72*10^{-6} x^2 + 1.02 x + 6190, \text{ i.e,}$$

$$M(H) = -4.72*10^{-6} H^2 + 1.02 H + 6190. \qquad (3.4.1)$$
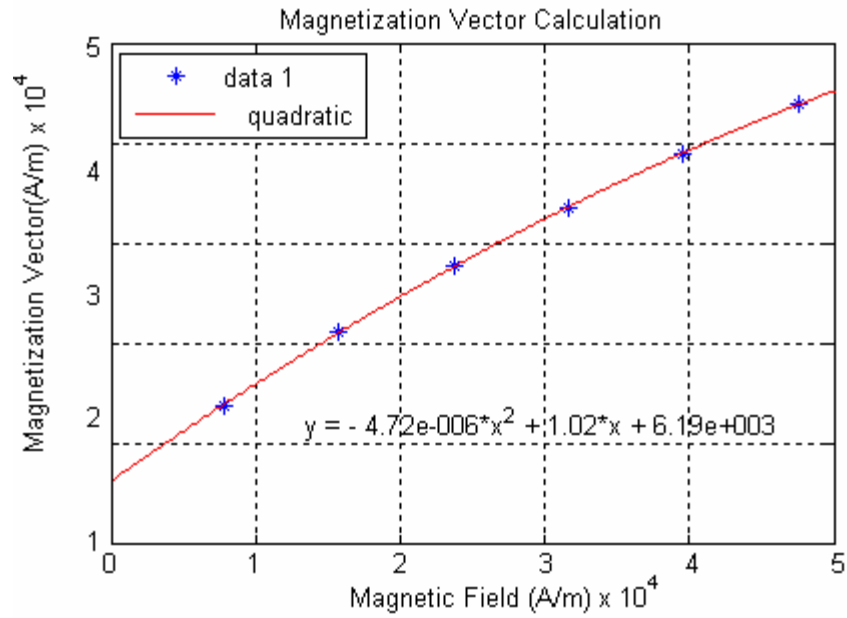
Figure 3.12: Quadratic equation of the dipole moment.

The magnetic field strength of the electromagnet at different distances away from its magnetic core was experimentally measured using a Gaussmeter (F. W. Bell 5080 Gaussmeter). The input current to the electromagnet was varied from 10mA to 360mA which produced magnetic fields of different strength. Thus obtained magnetic field strength is tabulated in Table 3.2.

With an appropriate unit conversion, magnetization vector for each magnetic field strength can be calculated using Eq. 3.4.1.

Table 3.2: Magnetic field strength of the electromagnet.

Input Current (mA)	H (Gauss) at 3mm	H (Gauss) at 4mm	H (Gauss) at 5mm
10	12.3	6.5	3.4
20	17.6	10	5.7
40	30	17.5	10.5
60	44.2	25.6	15.4
80	57	34.1	20.1
100	70.4	42.4	25.4
120	84.5	52	30.4
140	98.2	60.5	35.5
160	112.9	68.8	40.5
180	125	77	45.6
200	137.2	85.3	50.8
220	149.6	93.6	55.5
240	162.1	101.2	60.7
260	173.9	109.1	64.8
280	183.5	116.3	68.9
300	194.3	123.6	74
320	204	130.2	76.7
340	212	136.6	80.4
360	222	142.6	85.3

The experiment setup to measure the gradient of magnetic field strength is shown in Fig. 3.13. The magnetic field strength of electromagnet at each input current is

measured at different distance away from core. Second order polynomial equation is obtained using the curve fitting method. Then, the gradient of magnetic field strength is obtained by calculating the slope of polynomial equation.
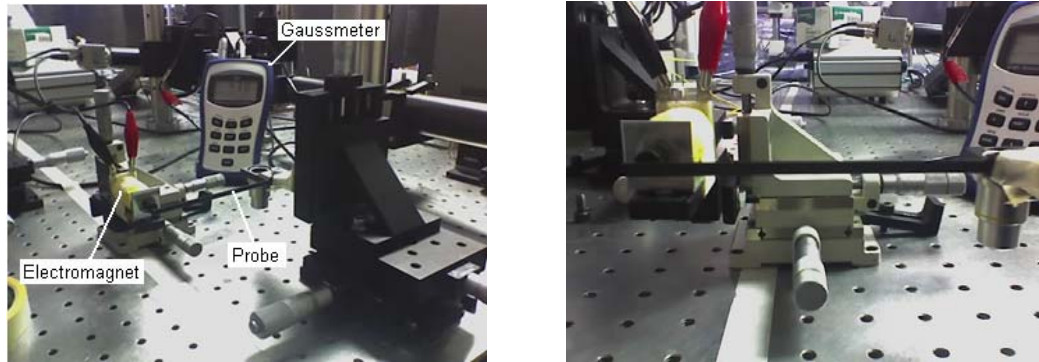
Figure 3.13: Experiment setup to measure the gradient of magnetic field strength.

The plot of magnetic field strength versus distance is shown in Fig. 3.14. It is important to note that the slope of the curve is negative. Thus, the gradient of magnetic field strength is negative. The absolute value of the gradient of field will be taken for the static and dynamic analysis (Case 1). The negative gradient simply means the measured magnetic field strength is in the opposite direction.

The magnetic field strength is also plotted with the negative direction and is shown in Fig. 3.15. The gradient of the field will thus be positive. The static and dynamic analysis will be performed using thus obtained gradient of field (Case 2).
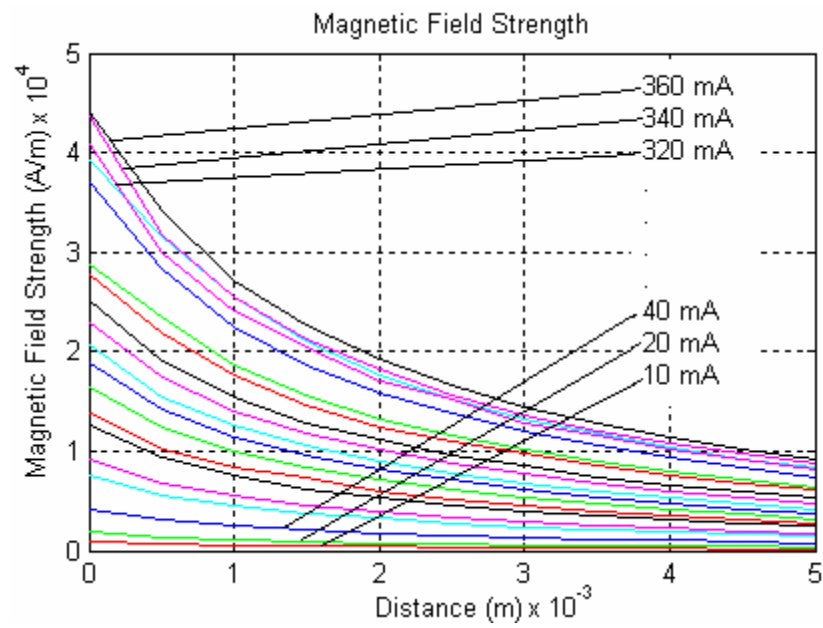
Figure 3.14: Plot of magnetic field strength with negative slopes.
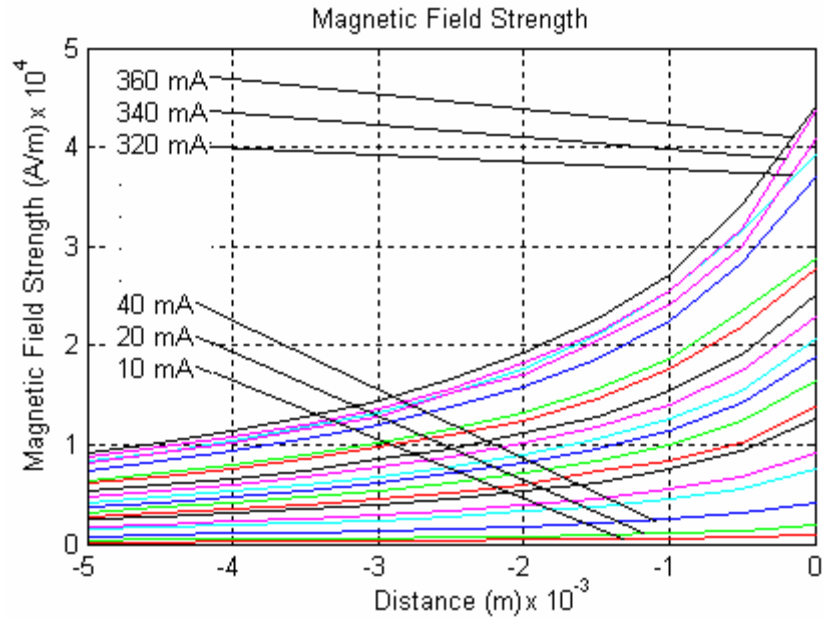
Figure 3.15: Plot of magnetic field strength with positive slopes.

3.4.3 Static and Dynamic Measurement

The experiment setup for the static and dynamic measurement is shown in Fig. 3.16. To perform static analysis, a DC voltage source is applied to the electromagnet, and a current meter is connected in series with the position sensitive detector to monitor the current generated. The current flowing into the electromagnet is also monitored using a current meter.

Experiments were carried out with two different lengths of fiber, 4.2 cm and 5.2 cm, with two different thicknesses of the gel, approximately 40 and 60 μm, respectively.
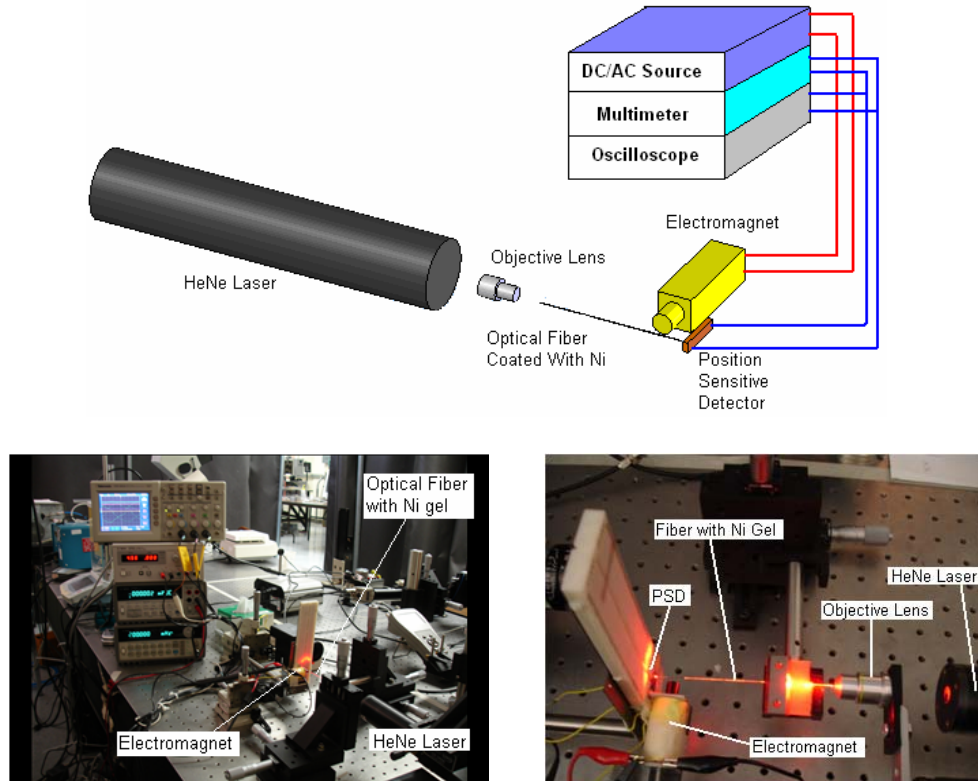
Figure 3.16: Experiment setup for static and dynamic measurement.

33

In this experiment, the end point of PSD is set as the origin. The photosensitivity of the PSD at the 632 nm wavelength of HeNe laser light is about 0.4 Amp/Watt and the beam spot on the PSD active area is about 0.3 mm in diameter which gives the current output from the PSD in the ranges of hundreds of μA.

The static data of displacement as a function of the magnetic field for the case 1 is shown in Fig. 3.17, 3.18 and 3.19. It can be seen from the figure that the theoretical and experimental result does not match. The discrepancy between the theoretical and experimental results is due to the fact that the measured magnetic field is in the opposite direction.
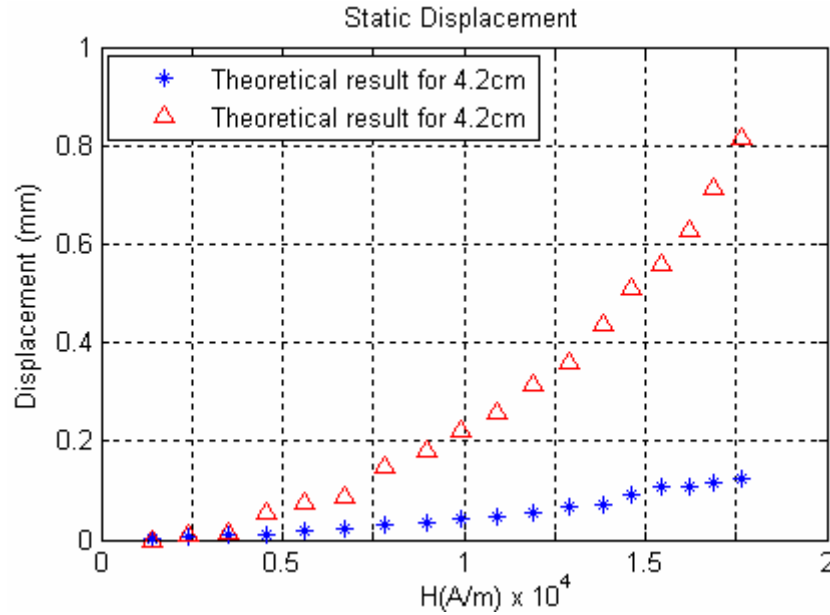
Figure 3.17: Static measurement results (Case 1) of 4.2 cm fiber.
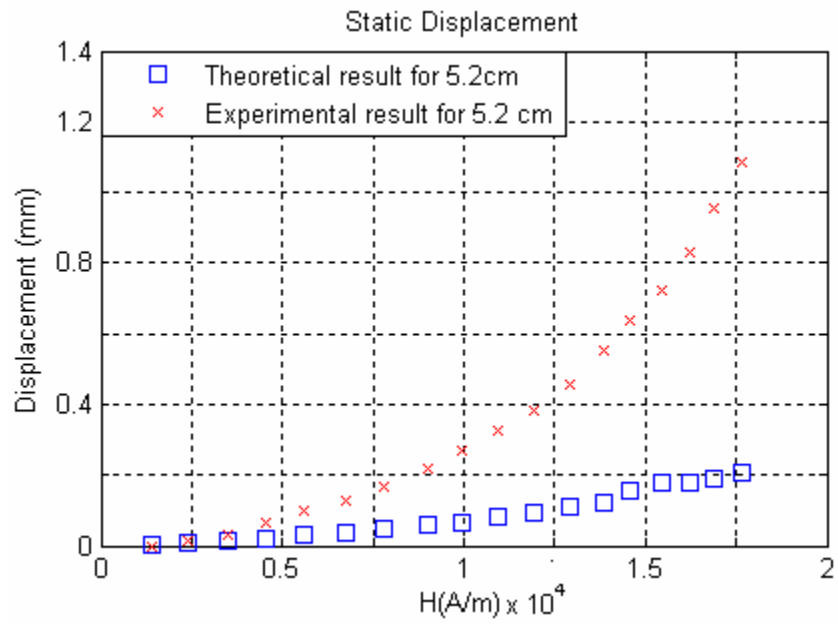
Figure 3.18: Static measurement results (Case 1) of 5.2 cm fiber.
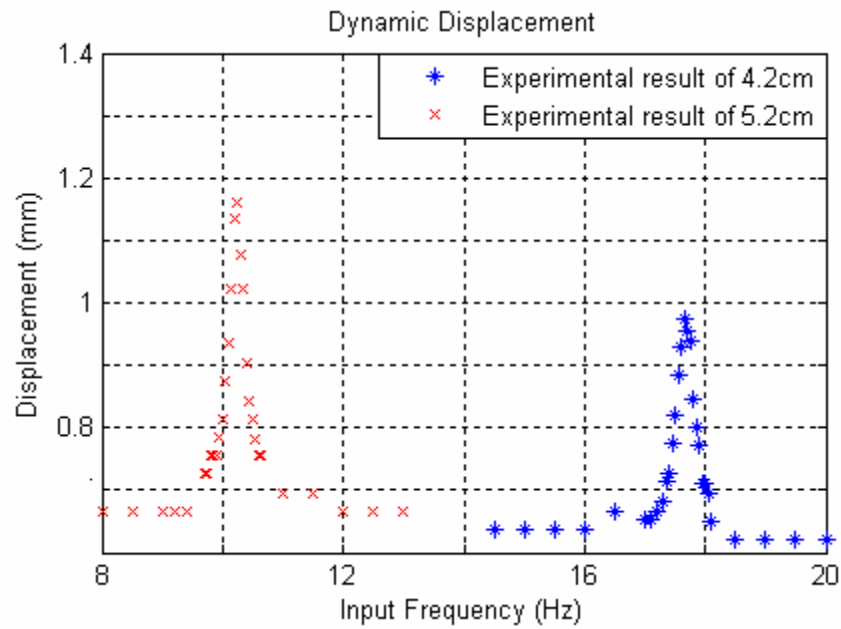
(c)

Figure 3.19: Dynamic measurement results (Case 1) of 4.2 and 5.2 cm fibers.

35
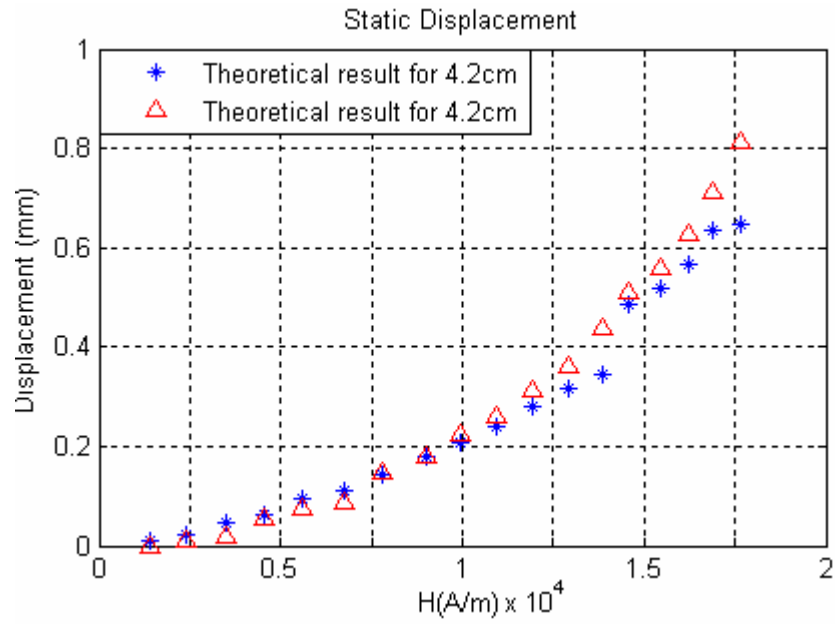
Figure 3.20: Static measurement results with 40 μm thick nickel gel (Case 2) of 4.2 cm fiber.
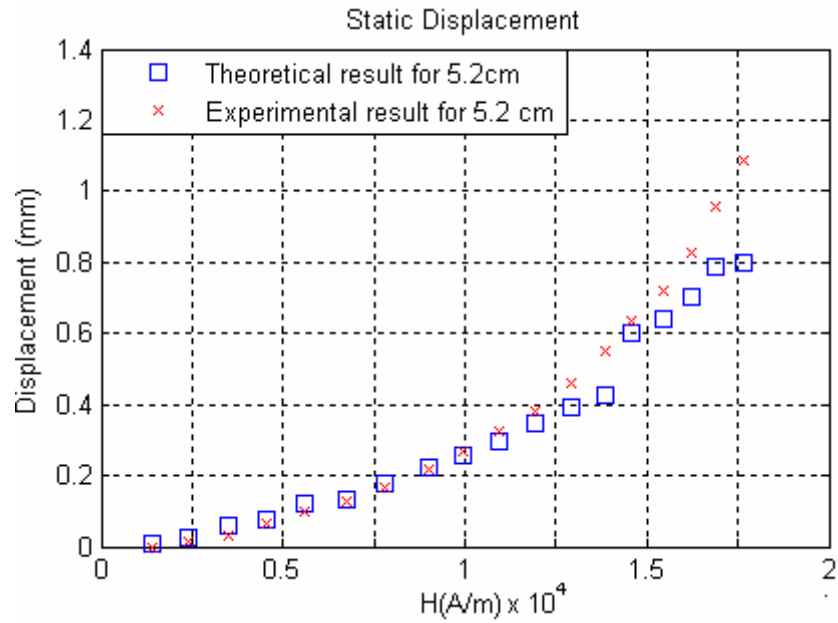
Figure 3.21: Static measurement results with 40 μm thick nickel gel (Case 2) of 5.2 cm fiber.
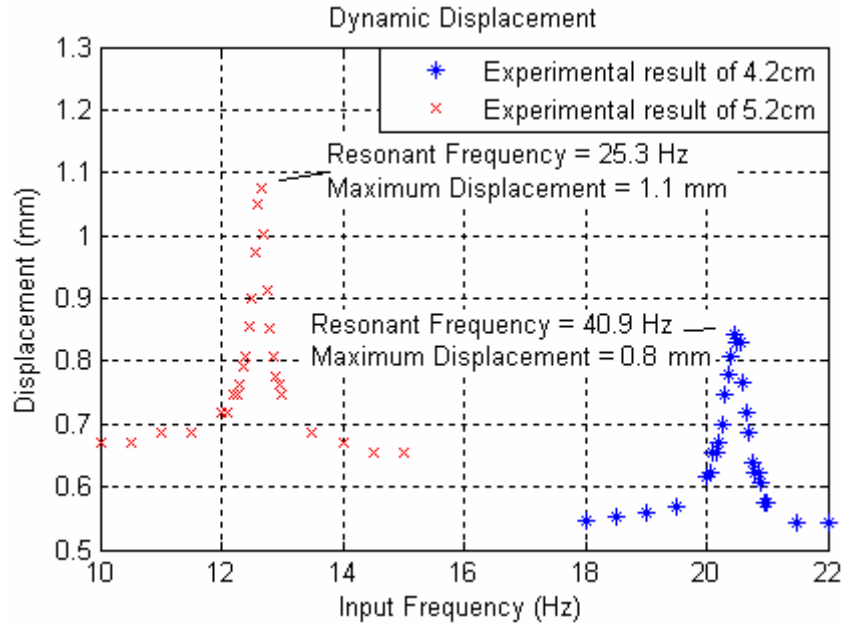
Figure 3.22: Dynamic measurement results with 40 μm thick nickel gel (Case 2) of 4.2 and 5.2 cm fibers.

The static data of displacement as a function of the magnetic field for the case 2 is shown in Fig. 3.20 and Fig. 3.23 for a fiber length of 4.2 cm, and Fig. 3.21, and Fig. 3.24 for a fiber length of 5.2 cm. It can be seen from the figure that the theoretical and experimental results are in good agreement. There are some discrepancies in the theoretical values for higher magnetic fields. This may be due to the fact that the magnetic field strengths at higher input currents to the electromagnet are not accurate. This inaccuracy arises due to the heating effect of the electromagnet. It can also be seen from the figure that the optical fiber displacement is nonlinear function of external magnetic field. Such nonlinearity is due to the magnetization vector M.

37
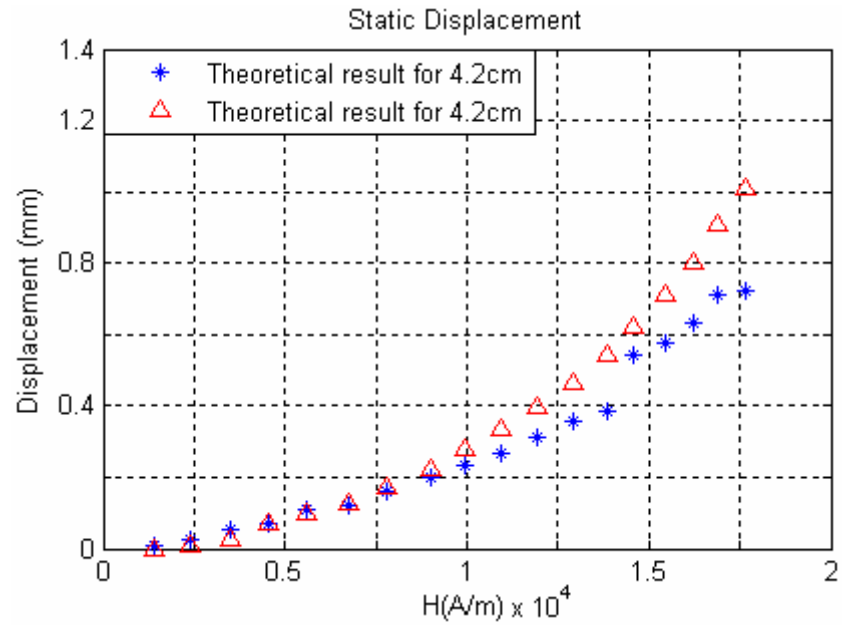
Figure 3.23: Static measurement results with 60 μm thick nickel gel (Case 2) of 4.2 cm fiber.
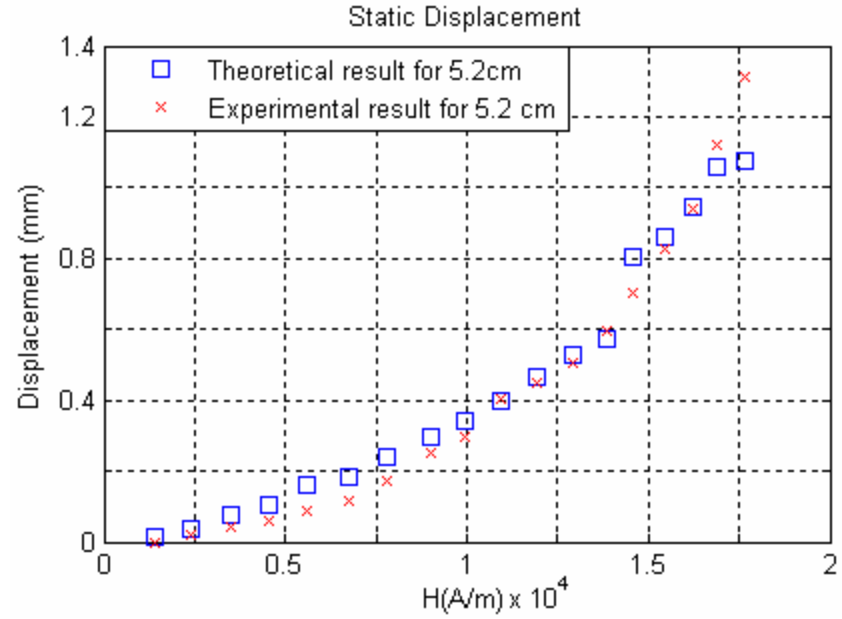
Figure 3.24: Static measurement results with 60 μm thick nickel gel (Case 2) of 5.2 cm fiber.
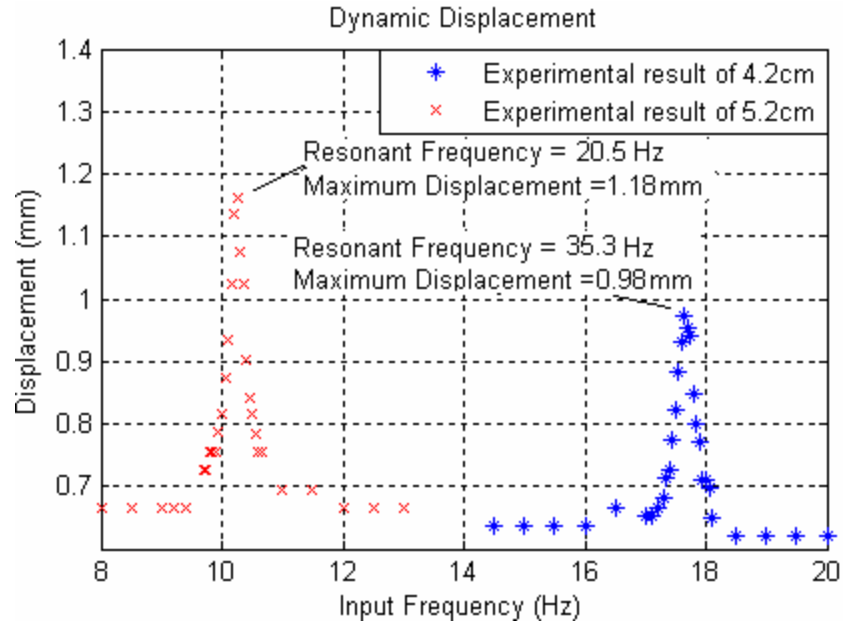
Figure 3.25: Dynamic measurement results with 60 µm thick nickel gel (Case 2) of 4.2 and 5.2 cm fibers.

For a 40 µm thickness of gel, the experimental values of static displacement of fiber is 0.81 mm for the 4.2 cm long fiber and 1.08 mm for the 5.2 cm long fiber at the input current of 360 mA and magnetic field strength of 17.66 KA/m. Theoretically, the values of static displacement re 0.64 mm and 0.75 mm respectively for 4.2-cm and 5.2-cm fibers. Similarly, for a 60 µm thickness of gel at the input current of 360 mA and magnetic field strength of 17.66 KA/m, the experimental values of static displacement of fiber are 1.01 mm and 1.24 mm for 4.2-cm and 5.2-cm fibers respectively. Theoretically, the values of static displacement are 0.75 mm and 1.03 mm respectively for 4.2-cm and 5.2-cm fibers. The difference in the theoretical and experimental value may be due to the measured magnetic fields at higher input currents because of the heating effect.

The fiber optic scanner is dynamically characterized by converting the PSD output currents to voltages by connecting a 100 KΩ resistor in series with each electrode of the PSD. The dynamic positions of the light spot can then be obtained by measuring the voltage waveform on an oscilloscope. Fig. 3.22 and 3.25 delineate the amplitude frequency response for 4.2-cm and 5.2-cm long fibers with 40 μm thick and 60 μm thick gel respectively. The figures show the dynamic response of optical fiber with lengths of 4.2 cm, and 5.2 cm with input current amplitude of 41 mA to the electromagnet and a magnetic field of 2.4 KA/m. For the 4.2-cm fiber with a 40-μm thickness of gel, the experimental value of dynamic displacement of fiber is 0.84 mm at the mechanical resonant frequency of 40.9 Hz. For a 5.2-cm long fiber, it is 1.07 mm at the mechanical resonant frequency of 25.3 Hz. Similarly, for a 4.2-cm long fiber with a 60-μm thickness of gel, the experimental value of dynamic displacement of fiber is 1.01 mm at the mechanical resonant frequency of 35.3 Hz. For the 5.2-cm fiber, it is 1.16 mm at the mechanical resonant frequency of 20.5 Hz. The dynamic response of the optical fiber is plotted as amplitude of the fiber as a function of input frequency. It can be observed from the dynamic response that the mechanical resonant frequency is twice the input frequency to the electromagnet. Theoretically, the resonant frequency of scanner can be calculated using Eq. 3.3.27.

$$f = \frac{1}{2\pi} \sqrt{\frac{3EI}{l^3 \left(M_g + 0.23 m_f \right)}}$$

The measured weight of optical fiber and ferromagnetic gel is listed in Table 3.3. Using these values and Eq. 3.3.27, the theoretical mechanical resonant frequencies

for 4.2-cm and 5.2-cm optical fibers with 40-µm thick ferromagnetic gel are 43.22 Hz and 28.72 Hz, respectively. Similarly, for 4.2-cm and 5.2-cm optical fibers with 60-µm thick

Table 3.3: Measured weights of fiber and ferromagnetic gel.

	Weight of Fiber (gm)	Weight of (Fiber+Gel) (gm)	Weight of Gel (gm)
2 Coat			
4.2	0.0012	0.0014	0.0002
5.2	0.0016	0.0018	0.002
3 Coat			
4.2	0.0012	0.0017	0.0005
5.2	0.0016	0.0021	0.0005

ferromagnetic gel, the mechanical resonant frequencies are 33.85 Hz and 23.23 Hz, respectively.

3.5 Finite Element Analysis

Finite element analysis has been performed to verify the theoretical and experimental results. For the static displacement simulation, the magnetic force at a specific magnetic field strength is calculated. The magnetic force thus obtained is applied to the fiber scanner model built in the ANSYS. The scanner model is meshed using a solid element called "SOLID186". Mechanical boundary condition is applied by

giving zero boundary condition to the free end of the model and a force is applied on the area where the nickel coating lies.

The calculated magnetic force for 40-µm thick nickel coating at an input current of 360 mA and a magnetic field strength of 17.66 KA/m is 23.49 µN, and that for 60-µm coating is 40.46 µN considering that 30% of the whole volume of gel is nickel. With these force applied to the scanner model, the static displacements obtained from ANSYS simulation are 0.73 mm and 1.06 mm for 4.2-cm and 5.2-cm fibers with 40-µm thick gel, respectively, as shown in Fig. 3.20 (a) and (b). Similarly, for 60-µm thick gel, the static displacements are 0.96 mm and 1.17 mm for 4.2-cm and 5.2-cm fibers, respectively, as shown in Fig 3.20 (c) and (d). The material properties used for the simulation is tabulated in Table 3.4.

Table 3.4: Material properties of optical fiber and nickel.

Material Properties	Optical Fiber	Nickel
Young's Modulus	72.39 Gpa	207 Gpa
Poisson's Ratio	0.28	0.31
Density	2.239 gm/cc	8.88 gm/cc
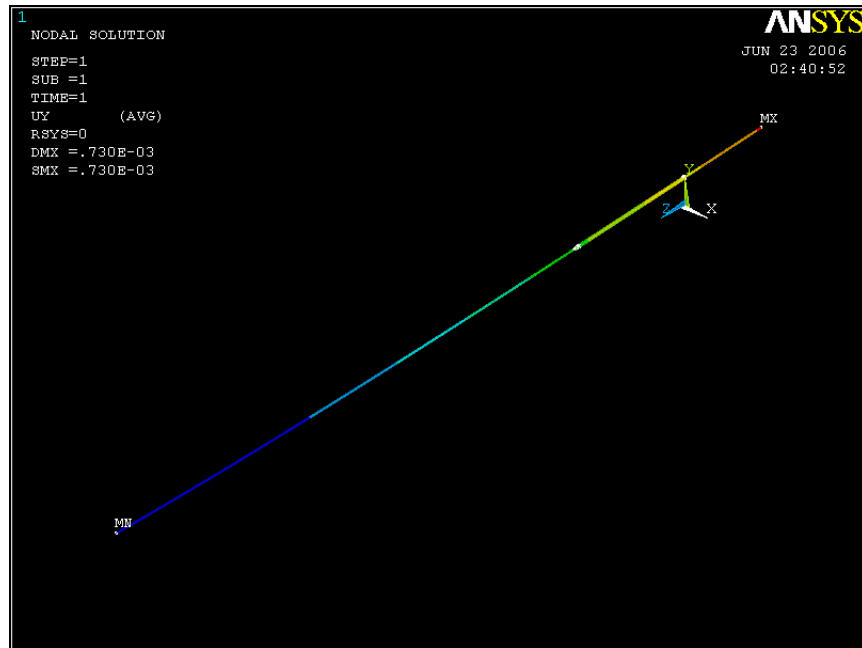
(a)
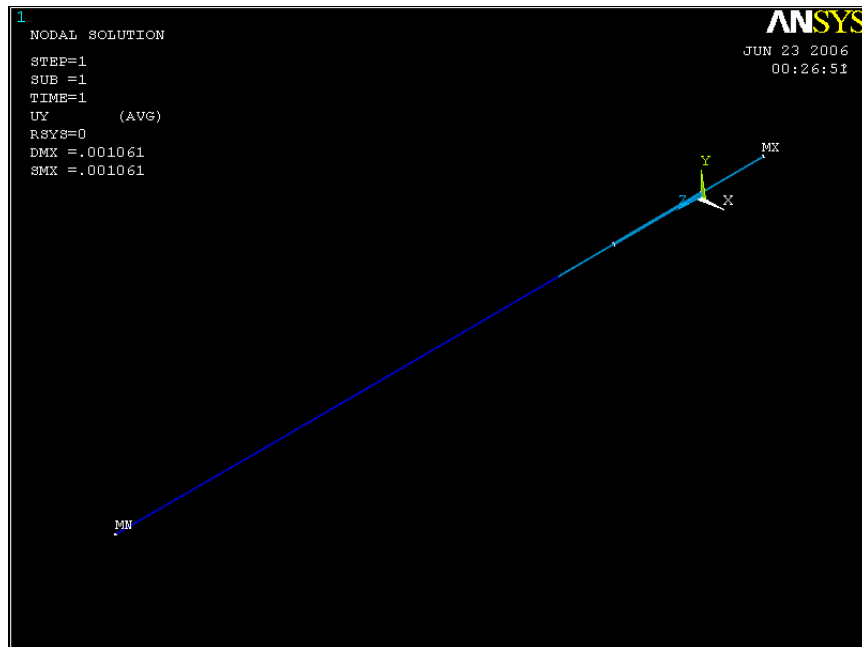
(b)

Figure 3.26: Static simulation of the fiber optical scanner with 40 µm thick nickel gel using ANSYS for (a) 4.2 cm fiber, and (b) 5.2 cm fiber.
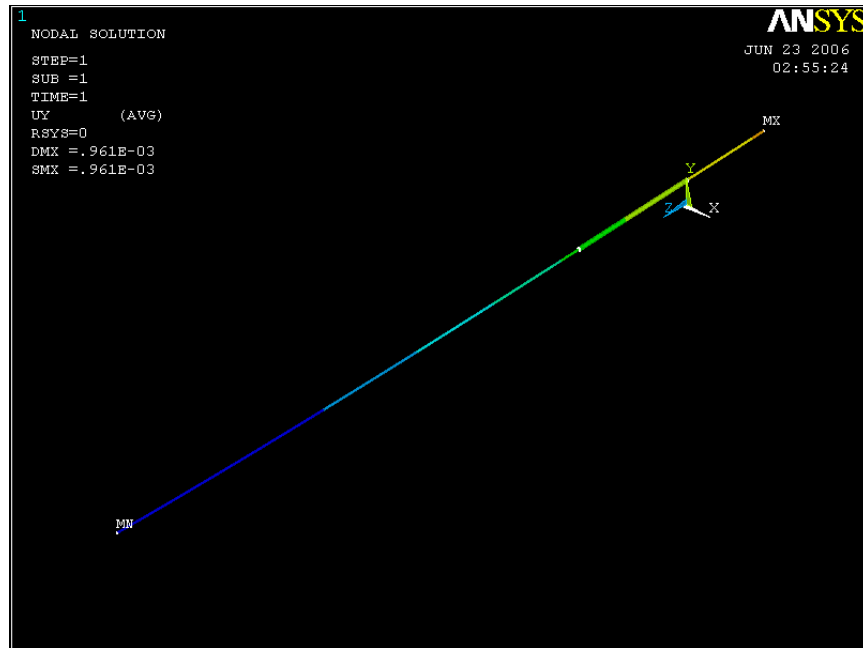
(a)
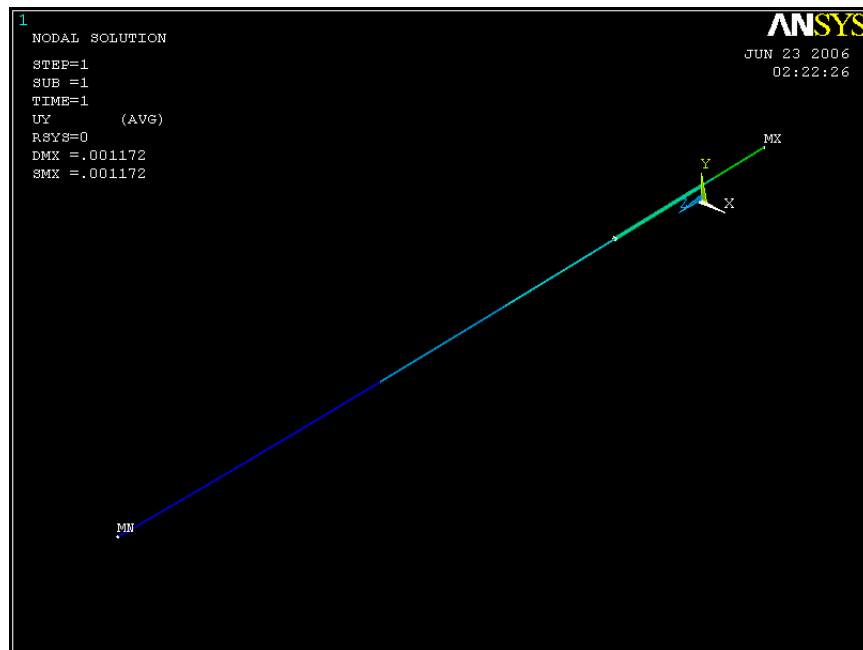
(b)

Figure 3.27: Static simulation of the fiber optical scanner with 60 μm thick nickel gel
using ANSYS for (a) 4.2 cm fiber, and (b) 5.2 cm fiber.

44
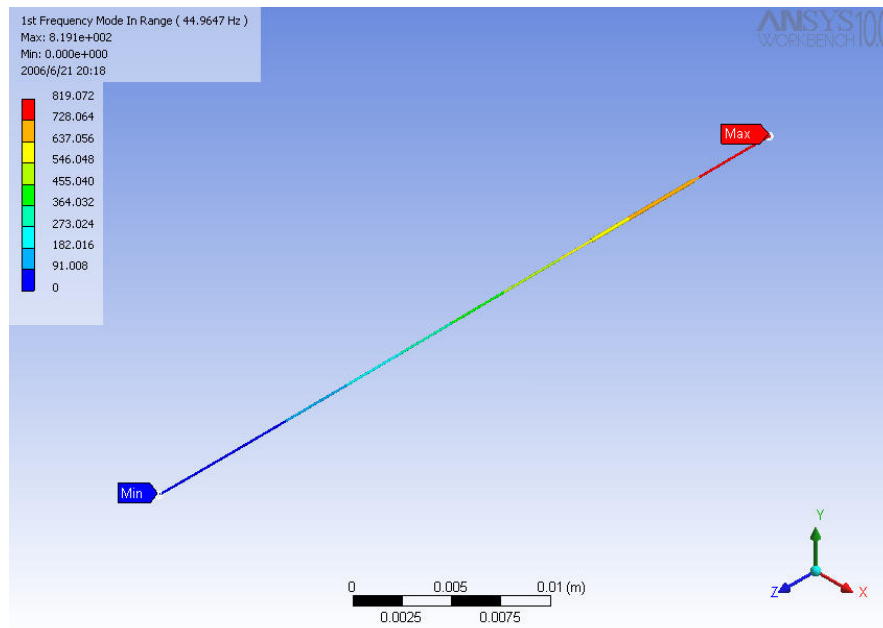
(a)
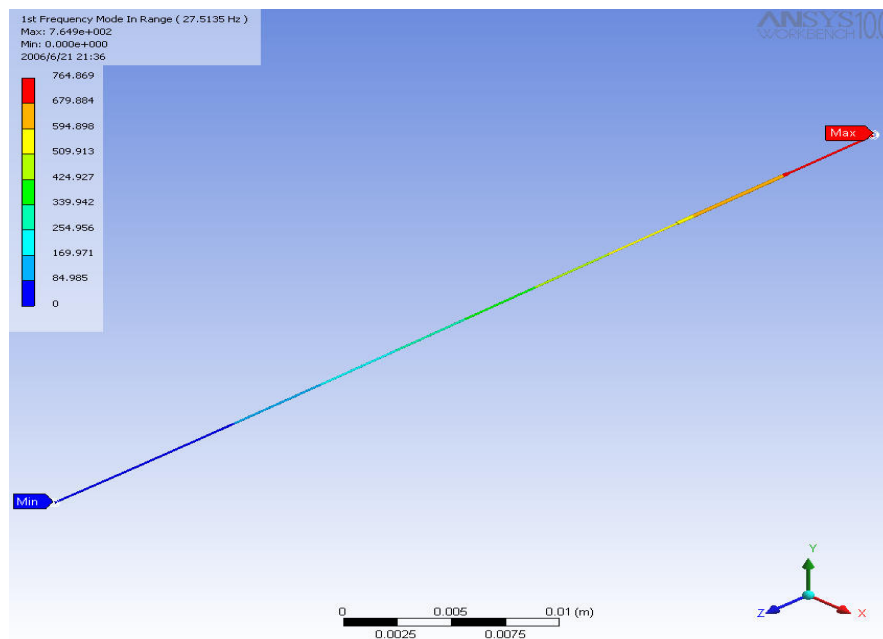
(b)

Figure 3.28 Resonant frequency simulation of fiber optical scanner with 40 µm thick nickel gel using ANSYS for (a) 4.2 cm fiber, and (b) 5.2 cm fiber.
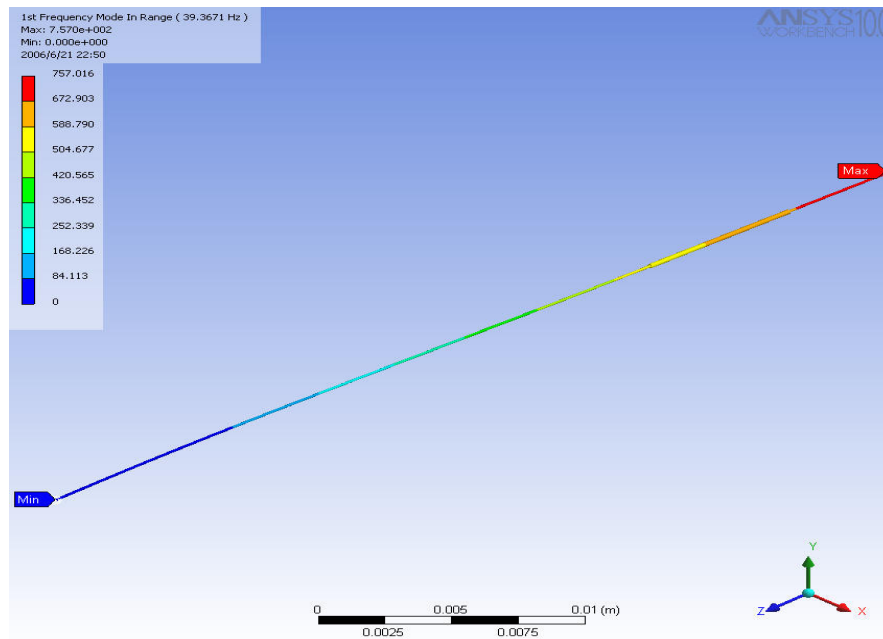
(a)
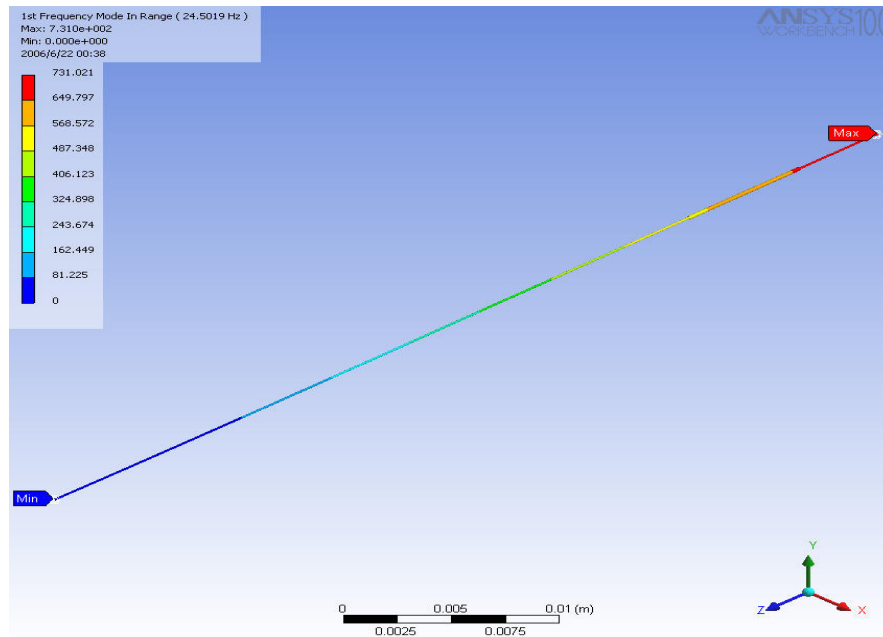
(b)

Figure 3.29 Resonant frequency simulation of fiber optical scanner with 60 µm thick nickel gel using ANSYS for (a) 4.2 cm fiber, and (b) 5.2 cm fiber.

The modal analysis in ANSYS is used to verify the theoretical and experimental resonant frequencies of the scanner. For simplicity, the effect of damping on the optical fiber due to air is not considered in the simulations. Fig. 3.28 (a) and (b) show the simulation results for 4.2-cm and 5.2-cm models with 40-µm nickel thickness. Similarly, Fig. 3.29 (a) and (b) show the simulation results for 4.2-cm and 5.2-cm model with 60-µm nickel thickness. The simulation results are in good agreement with the theoretical values. Comparison of theoretical, experimental and simulation results of static displacement, and resonant frequencies are listed in Table 3.5.

Table 3.5: Comparison of theoretical, experimental and simulation result.

4.2 cm with 40 µm Coating	Theoretical	Experimental	Simulation
Static Displacement	0.64 mm	0.81 mm	0.73 mm
Resonant Frequency	43.22 Hz	40.9 Hz	44.96 Hz
4.2 cm with 60 µm Coating			
Static Displacement	0.75 mm	1.01 mm	0.961 mm
Resonant Frequency	33.85 Hz	35.3 Hz	39.36 Hz
5.2 cm with 40 µm Coating			
Static Displacement	0.8 mm	1.08 mm	1.061 mm
Resonant Frequency	28.72 Hz	25.3 Hz	27.51 Hz
5.2 cm with 60 µm Coating			
Static Displacement	1.03 mm	1.24 mm	1.172 mm
Resonant Frequency	23.23 Hz	20.5 Hz	24.50 Hz

3.6 Conclusions

In this chapter, a 1-D fiber optic scanner based on electromagnetic actuation was introduced. A brush coating technique was implemented to coat a thin ferromagnetic material on single-mode optical fibers. The static and dynamic characterization of the scanner was performed. The scanner is capable of 0.81 mm linear displacement under the influence of a static magnetic field of 17.6 KA/m in a fiber with a moveable length of 4.2cm. Dynamically, it is capable of a linear displacement of 0.83mm with input current amplitude of 41mA and a magnetic field of 2.4 KA/m. The theoretical and experimental results were verified using the finite element analysis. The principle and design were demonstrated. The fiber length, coating thickness and magnetic field strength can be chosen depending on the imaging needs. This device can be implemented for the optical coherence tomography for *in vivo* imaging of tissues and organs since there is no current and voltage inputs to the *in vivo* device.

CHAPTER 4

A CANTILEVER-TYPE ZIPPER ACTUATOR

4.1 Introduction

The fields of optical MEMS (Micro-Electro-Mechanical Systems) and optical microsystems are at a fast growing stage. Optical MEMS has become a promising technology in the fields of telecommunication, high-resolution display, and medical imaging. MEMS scanners used to redirect an optical beam are specially explored for medical imaging systems where high-resolution, nondestructive, and real time imaging is critical. MEMS scanners offer more compact design, and low power consumption with potential lower costs. They require optically flat mirrors, moderate actuation voltages, and high reliability. For high resolution imaging, a large mirror area and a wide scan range are critical aspects, and three dimensional medical imaging requires a 2-D scanning.

The technologies used to fabricate MEMS scanners include SOI (silicon on insulator), bulk micromachining, and surface micromachining. All can be done monolithically using conventional semiconductor process. Therefore, the fabrication costs could be lower than those for mechanical mirrors. Various actuation mechanisms have been used to actuate the MEMS scanners such as electromagnetic, electrostatic, thermal, and piezoelectric.

In this section, design of a surface micromachined cantilever-type zipper actuator is presented. This actuator can be utilized to design a 2-D scanner. The scanner can be used for *in vivo* or *ex vivo* imaging. The actuation principle of the zipper actuator is based on the electrostatic force between a curved cantilever and a bottom electrode that pulls the cantilever down. The 3-D imaging is made possible by implementing four such zipper actuators. The zipper actuator is characterized statically and dynamically. In this thesis, the design consideration in displacement, electrostatic force, and electrostatic stability of the zipper actuator is presented. The finite element analysis is used to verify the static and dynamic results. The general description of the zipper actuator based 2-D scanner is presented in the section 4.2. The principle of operation, lumped modeling analysis, experimental results and finite element analysis of zipper actuator are addressed in the section 4.3.

4.2 General Description of Zipper Actuator Based 3D Scanner

The schematic of complete 2-D OCT scanner is shown in Fig. 4.1. The device can be packaged in an acrylic package that can provide mechanical support and protection in *in vivo* or *ex vivo* environment [22]. The package consists of concentric holes with same center point along the central axis for the precise alignment of the optical fiber, lens and the MEMS mirror. The MEMS mirror is mounted on a 45° platform to redirect the light beam.

50
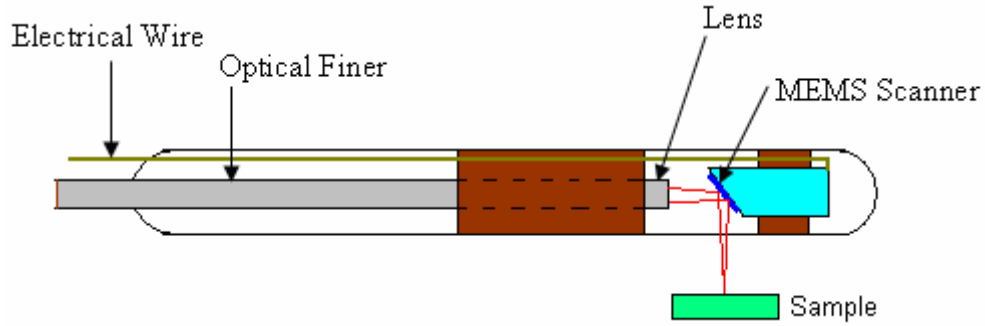
Figure 4.1: Schematic of complete thermal actuator based 2D scanner.

The packaged probe can be integrated with fiber based OCT system as shown in Fig. 2.1 to focus the light into a sample, and to collect the reflected light. The reflected light from sample and the reference can then be combined to acquire the sample image.

4.3 Modeling and Analysis of Zipper Actuator

Electrostatic actuators are widely used in the microelectromechanical systems. Electrostatic actuators show advantages of low power consumption, high actuation speeds, and fabrication compatibility [53]. Both large deflection and high force can be achieved by using the cantilever type electrostatic zipping actuator. Electrostatic actuators with an S-shaped film element and deformed membrane have been reported with high displacements [54, 55]. Legtenberg *et al.* have demonstrated laterally compliant curved electrode zipping actuators [56]. Curved electrode has been used in microactuators to align optical fibers [57]. A large gap between the top and the bottom electrode increases the voltage required to actuate the actuator. The zipping actuator works well if the gap between the both electrodes is small at the beginning of zipping

action [58]. The zipper actuator can be fabricated using various commercial fabrication processes such as DRIE and surface micromachining.

The actuator was designed to achieve high displacements and fabricated using the multi-layer polysilicon foundry fabrication process PolyMUMPS. Previous electrostatic zipper actuators require a thin layer of dielectric material on top of the bottom electrode to prevent electrical shorting. They may have an issue with electrical breakdown of the thin dielectric layer due to the film quality. A new mechanical structure has been designed to avoid the electrical shorting problem without a layer of dielectric material. Our analysis and experimental results demonstrated that the design can withstand high voltages without shorting and is capable of high deflections. The vertical displacements of various devices configurations were found ranging from 26 μm to 450 μm while the actuation voltages varied in the range of 12 V to 45.3 V for complete actuation. Pull-in voltages for various configurations were analyzed and presented.

Modeling and analysis of the cantilever-type zipper actuator is presented in this section. The subjects will be discussed in the order of principle of operation, lumped modeling analysis, experimental results, and finite element analysis.

4.3.1 Principle of Operation

The L-Edit mask layout and the actuator after HF release of the curved cantilever-type electrostatic zipper actuator are shown in Fig. 4.2 (a), and (b). After the HF release process, the top electrode curves up due to the bending stress and thermal expansion of the polysilicon and metal layers.

52
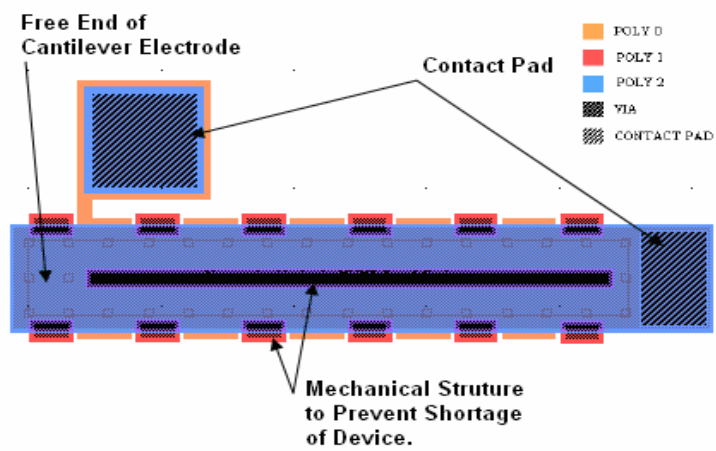
(a)
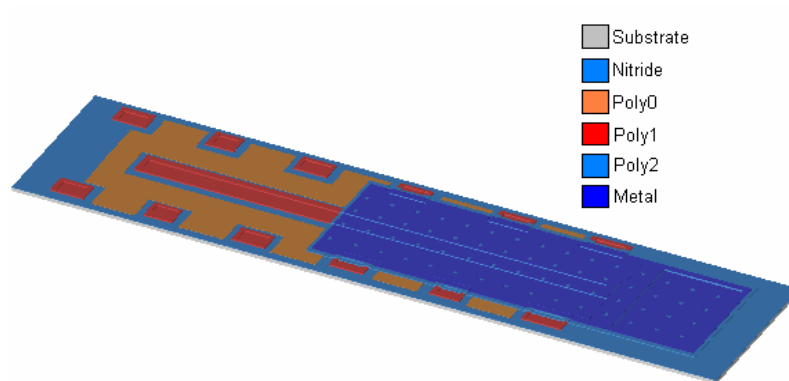
(b)
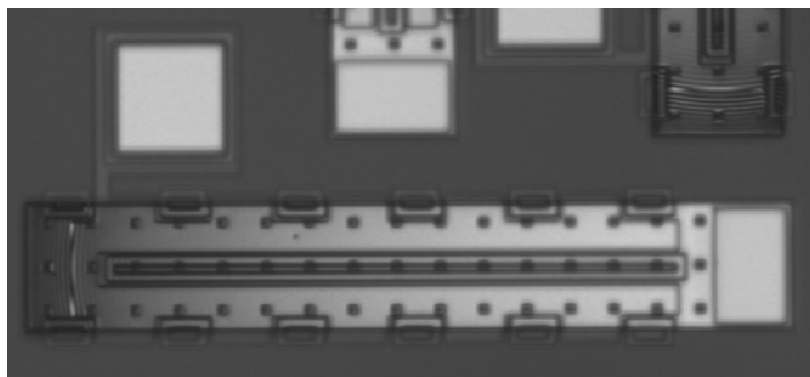
(c)

Figure 4.2: Cantilever type electrostatic zipper actuator. (a) L-Edit mask layout. (b) Detail view of mechanical structure. (c) Device after HF release.

When the voltage is applied on the contact pad, the electrostatic force between the curved cantilever and the bottom electrode on the substrate pulls the cantilever down. With a warped cantilever, the force closes the gap from the anchor end and gradually the zipping effect actuates the entire cantilever without increasing the biasing voltages. Conventional electrostatic actuator uses a dielectric layer such as thermal oxide or nitride to prevent an electrical short circuit between the top and bottom electrodes when the top electrode is pulled down. In this design, mechanical structure shown in Fig. 4.2 has been added to prevent the top electrode from coming in contact with the bottom electrode, thus preventing electrical shortage.

4.3.2 Lumped Modeling Analysis

The lumped modeling analysis and the behavior of the actuator are presented in this section. Various aspects such as stress induced bending of the cantilever beam, electrostatic force and the pull-in voltage of the actuator will be discussed, and the design considerations for higher displacement will be presented.

4.3.2.1 Stress induced bending

Micromachined cantilever beams are subject to residual stresses due to the fabrication process [59, 60]. This stresses causes the cantilever beam to curl upwards. During the HF release process, the MUMPs chips are heated, and the cantilever beams deflects fully downwards touching the substrate. Upon returning to the room temperature, the cantilevers curve up more than the stress-induced state. The schematic of the cantilever beam is shown in Fig. 4.3 with thickness' of h_1 and h_2, residual stress of σ_1 and σ_2, and Young's modulus of E_1 and E_2 for polysilicon and gold layers

54

respectively. The force and moments acting on the structure are also shown in the figure [61].

The internal forces at any cross section of the beam must be in equilibrium. Therefore,

$$P_1 = P_2 = P \qquad (4.3.1)$$

$$\frac{P(h_1 + h_2)}{2} = M_1 + M_2 \qquad (4.3.2)$$
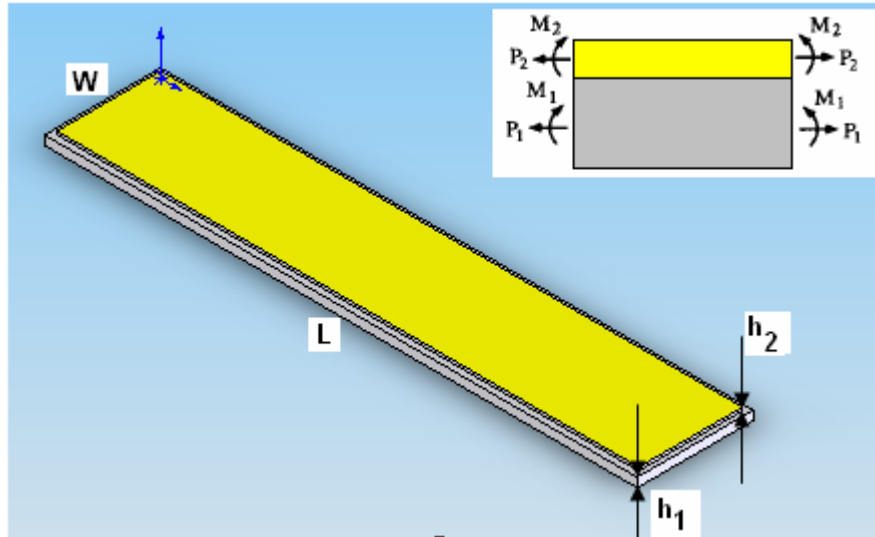

Figure 4.3: Schematic of the cantilever beam.

$$\frac{P(h_1 + h_2)}{2} = \frac{E_1 I_1}{\rho} + \frac{E_2 I_2}{\rho} \qquad (4.3.3)$$

Where P_1 is tensile force on polysilicon, P_2 is compressive force on gold, M_1 and M_2 are bending moment acting on polysilicon and gold respectively, I_1 and I_2 are area moment of inertia of polysilicon and gold respectively.

55

The strain in both gold layer and polysilicon layer depends on residual stress, axial force and radius of curvature. At the interface of the two layers, the strains of both layers are in equilibrium. Therefore, at the interface,

$$\frac{\sigma_1}{E_1} + \frac{P}{E_1 h_1 w} + \frac{h_1}{2\rho} = \frac{\sigma_2}{E_2} - \frac{P}{E_2 h_2 w} + \frac{h_2}{2\rho} \qquad (4.3.4)$$

where w is width of the cantilever beam.

From Eq. 4.3.3 and 4.3.4, the radius of curvature of the cantilever solely due to the residual stress is given by

$$\rho = \frac{\left(w_1 E_1 h_1^2\right)^2 + \left(w_2 E_2 h_2^2\right)^2 + 2 w_1 w_2 E_1 E_2 h_1 h_2 \left(2 h_1^2 + 3 h_1 h_2 + 2 h_2^2\right)}{6 w_1 w_2 E_1 E_2 h_1 h_2 \left(h_1 + h_2\right)\left(\dfrac{\sigma_2}{E_2} - \dfrac{\sigma_1}{E_1}\right)} \qquad (4.3.5)$$

And the total deflection at the tip of free end of cantilever is

$$d = \rho\left(1 - Cos\left(\frac{L}{\rho}\right)\right) \qquad (4.3.6)$$

where L is length of the cantilever beam.

The total deflection due to the residual stress and curing temperature ∇T can be obtained from Eq. 4.3.3 [62] where,

$$\frac{P(h_1 + h_2)}{2} = \frac{E_1 I_1}{\rho} + \frac{E_2 I_2}{\rho} \qquad (4.3.7)$$

And at the interface of the two layers,

$$\alpha_1 \Delta T + \frac{P}{E_1 h_1 w_1} + \frac{h_1}{2\rho} = \alpha_2 \Delta T - \frac{P}{E_2 h_2 w_2} - \frac{h_2}{2\rho} \qquad (4.3.7)$$

where, w_1 and w_2 are the width of polysilicon and gold layers, respectively, and α_1 and α_2 are thermal expansion coefficients of polysilicon and gold layers, respectively. From

Eq. 4.3.7 and 4.3.8, the radius of curvature due to the residual stress and curing temperature is given by

$$\rho = \frac{\left(w_1 E_1 h_1^2\right)^2 + \left(w_2 E_2 h_2^2\right)^2 + 2w_1 w_2 E_1 E_2 h_1 h_2 \left(2h_1^2 + 3h_1 h_2 + 2h_2^2\right)}{6w_1 w_2 E_1 E_2 h_1 h_2 \left(h_1 + h_2\right)\left(\alpha_2 - \alpha_1\right)\Delta T} \qquad (4.3.9)$$

The total deflection of the cantilever can be calculated using Eq. 4.3.6, and a MatLAB code to solve for the total stress induced deflection and the deflection due to the residual stress and curing temperature. For cantilever electrode of 475 μm long and 90 μm wide, the total deflection solely due to stress is 16.285 μm. In our calculations, the induced stress due to fabrication processes was taken from the PolyMUMPs database which is 7.8MPa for polysilicon and 23.3MPa for the gold layer. Similarly, the deflection due to the residual stress and curing temperature is found to be 34.334 μm at a curing temperature of 100°C and room temperature of 30°C.

It is evident from Eq. 4.3.6 and 4.3.9 that increase in the curing temperature will increase the total deflection of the cantilever electrode. The MatLAB was used to plot the total deflection at various curing temperatures for a cantilever electrode with a length of 475 μm and a width of 90 μm. This is shown in Fig.4.4. The plot shows a linear relationship between the curing temperature and the total deflection.
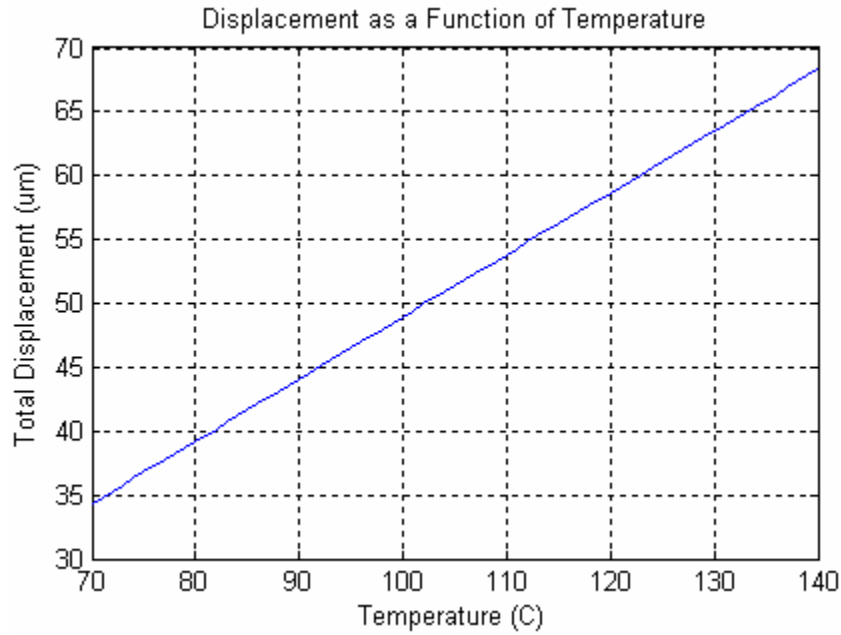
Figure 4.4: Displacement as a function of temperature.

4.3.2.2 Electrostatic force

A general analysis of the electrostatic force of the cantilever-type zipper actuator can be performed by considering a parallel plate capacitor configuration composed of a moveable plate of a mass M and a spring constant K separated from the bottom electrode by an air gap d_o [63]. The configuration is shown in Fig. 4.5. A constant voltage is applied between the top and bottom electrodes. Electrical energy is stored in the electric fields established by the charges accumulated in the capacitor due to the applied electric potential. The electrostatic force due to the charges stored in the capacitor pulls the top electrode towards the bottom electrode causing the top electrode to deflect. This electrostatic force is inversely proportional to the air gap between the

top and bottom electrode, and therefore it is highly nonlinear. For lumped modeling analysis, damping within the system was neglected.
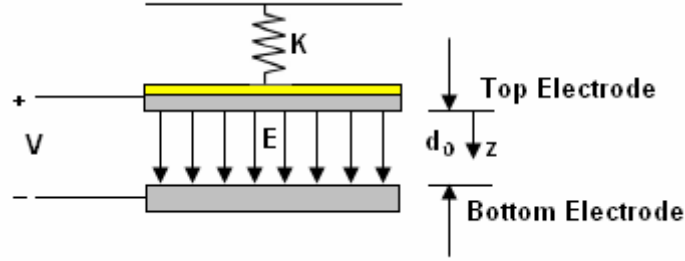
Figure 4.5: Parallel plate configuration of a zipper actuator.

The equation of motion of the top electrode due to electrostatic force is

$$F_{electrostatic} = M \frac{d^2 z}{dt^2} + F_{mechanical} \qquad (4.3.10)$$

The electrostatic force due to stored charge is

$$F_{electrostatic} = \frac{\varepsilon_0 A V^2}{2(d_0 - z)^2} \qquad (4.3.11)$$

Where, A is the area of moveable plate, ε_0 is the permittivity of free space, d_o is the initial gap between the top and bottom electrodes, z is the displacement, and V is the applied potential.

4.3.2.3 Pull-in voltage

The pull-in action is related to the elastic and electrostatic forces. When electric potential is applied between the two electrodes, the electrostatic force generated causes the top electrode to collapse towards the bottom electrode. The elastic force is a linear

function of the top electrode displacement. In contrary, the electrostatic force is inversely proportional to the air gap between the two electrodes. When the applied voltage is increased, the top electrode slowly snaps towards the bottom electrode. At a certain input voltage, the electrostatic force becomes larger than the elastic force when the system can not reach a force balance causing the top electrode to collapse to the bottom electrode. This phenomenon is called pull-in. And the voltage at this point is called the pull-in voltage.

Chowdhury *et al.*[64] have formulated a closed-form expression for the pull-in voltage:

$$V_{PI} = \sqrt{\frac{2\,\tilde{E}\,h^3\,d_0}{8.37\,\varepsilon_0\,l^4\left(\dfrac{5}{6d_0^{\,2}} + \dfrac{0.19}{d_0^{\,1.25}w^{0.75}} + \dfrac{0.19}{d_0^{\,1.25}l^{0.75}} + \dfrac{0.4h^{0.5}}{d_0^{\,1.5}w}\right)}} \qquad (4.3.12)$$

$$\tilde{E} = \frac{E}{1-v^2} \qquad (4.3.13)$$

where, E is the Young's modulus and v is the Poisson ratio.

This formulation assumes that the top electrode has only one layer. The top electrode of a zipper actuator in this thesis has two layer, 0.5-μm thick gold layer deposited on top of a polysilicon layer. The Young's modulus of polysilicon is 168GPa and that of gold is 77.2GPa [64].
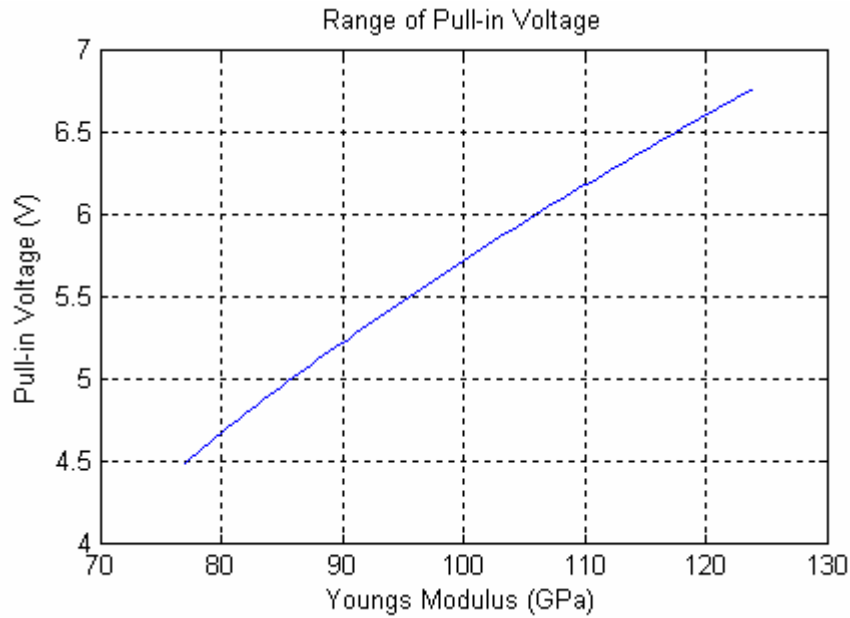
Figure 4.6: Range of the pull-in voltages.

Assumption can be made that if the thickness of polysilicon is very small, the Young's modulus of gold can be used for calculation. The Young's modulus of polysilicon can be used for calculation if the thickness of gold is comparably small. Therefore, it can be assumed that the Young's modulus of the bi-layer cantilever is between 77.2GPa and 168GPa. With these values, a MatLAB was used to plot the range of the pull-in voltage for the cantilever actuator with a length 475 μm and a width of 90 μm, as shown in Fig. 4.6. These values indicate the pull-in voltage should be in the range of 4.5 V to 6.7 V.

4.3.3 Finite Element Analysis

Finite element analysis was used to validate the theory presented in the section 4.3.3. ANSYS and FemLAB have been used for the simulation. A three dimensional

61

model was built in Solidworks and then imported to ANSYS and FemLAB. The residual stress is assumed to be uniformly distributed. The "Solid, stress-strain" available in the MEMS module is used in the FemLAB simulation for the stress induced deformation. The simulation result is shown in Fig. 4.7. The total deflection obtained from simulation is 16.29 µm which is in good agreement with the theoretical value of 16.285 µm. For the deflection due to the residual stress and curing temperature, the cantilever structure is meshed with a solid element called "Solid186". A sequential simulation is performed where the beam is first subjected to the stress. The deformed structure thus obtained is heated to 100°C and then brought back to the room temperature. The simulation result is shown in Fig. 4.8.
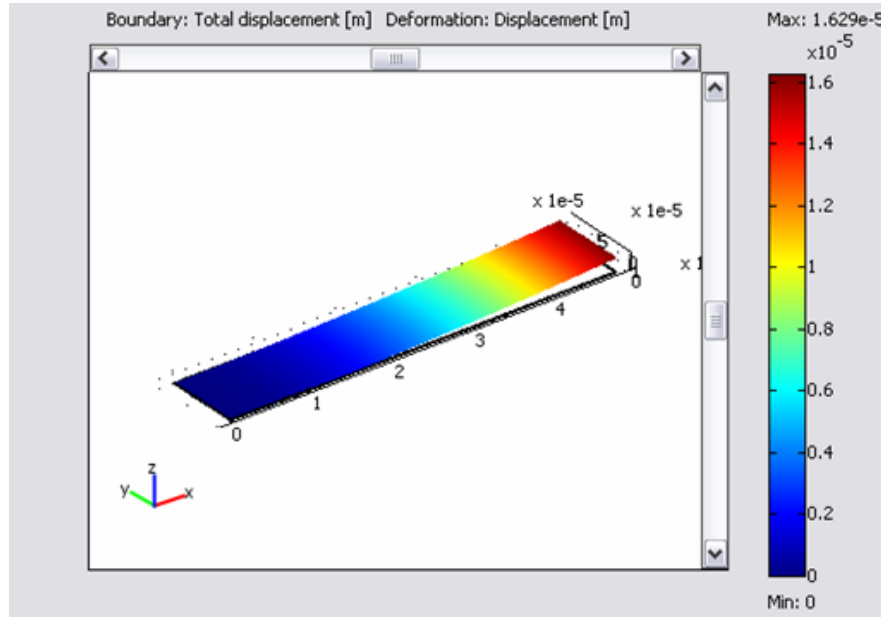
Figure 4.7: Stress induced deflection of a zipper actuator.
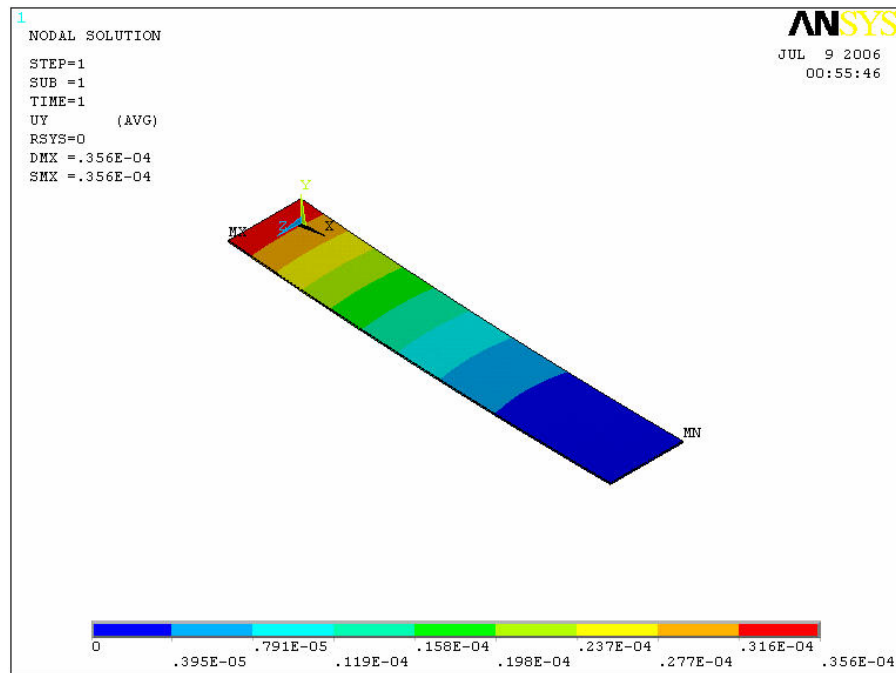
Figure 4.8: Deflection due to the residual stress and curing temperature.
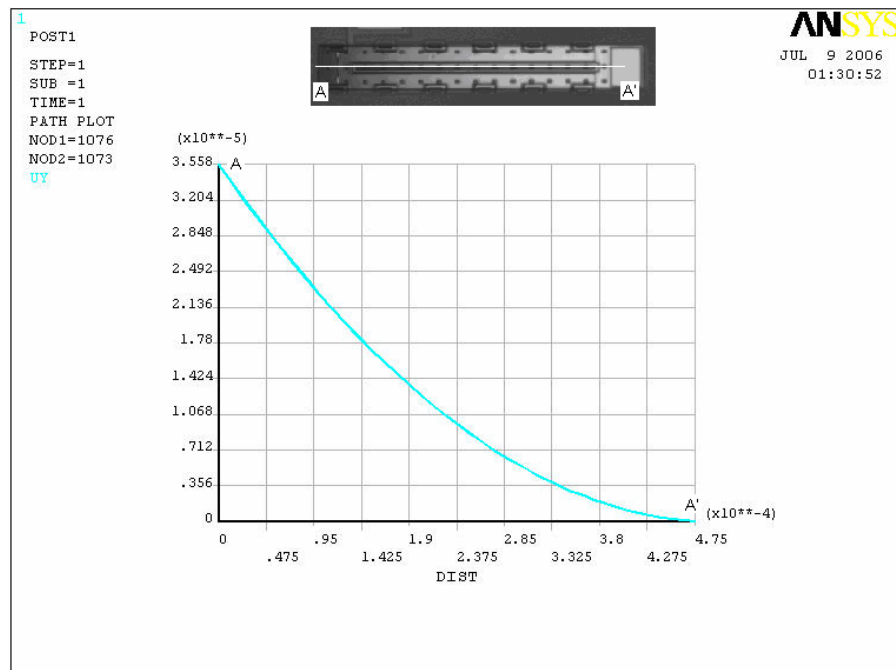
Figure 4.9: Curvature of the top electrode.

63
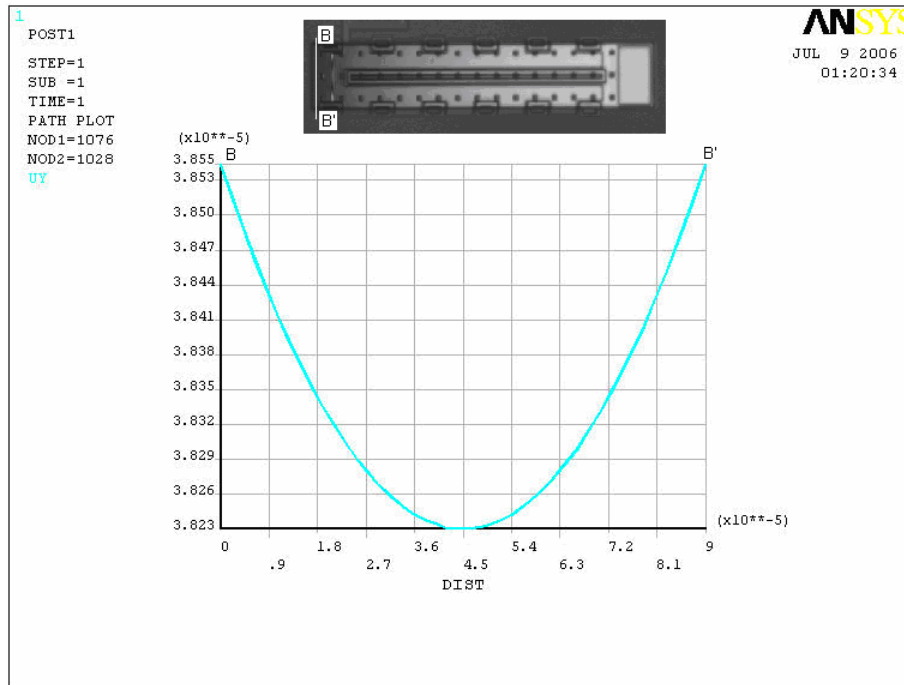
Figure 4.10: Curvature of the free end of top electrode.

The total deflection due to the residual stress and change in temperature obtained from simulation is 35.58 µm which is in good agreement with the theoretical value of 34.334 µm. Fig. 4.9 shows the curvature along the length of the electrode and Fig. 4.10 shows the curvature along the width of the free end of cantilever. The curvature along the width increases with increase in the width. Therefore, the top electrode design can be optimized to obtain a desired curvature along the width so as to prevent the electrical shorting of the device.
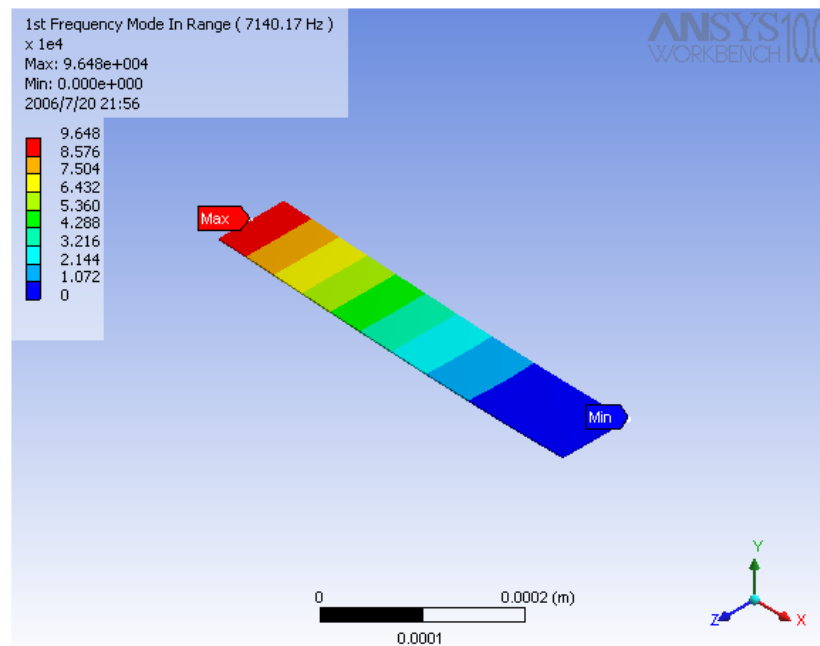
(a)
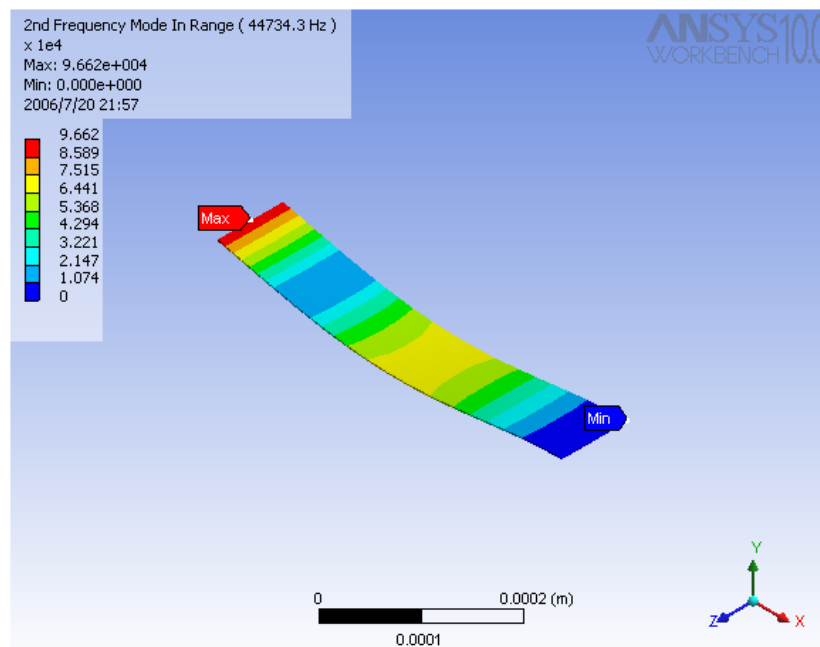
(b)

Figure 4.11: A mechanical resonant frequency of a zipper actuator. (a) First mode. (b) Second mode.

Modal analysis was performed to obtain the resonant frequency of a zipper actuator. The first and second mode of a mechanical resonant frequency is 7.14 KHz and 44.734 KHz, respectively. The simulation result is shown in Fig. 4.11.

4.3.4 Experimental Results

Zipper actuator with various lengths and widths were fabricated using the MUMPs process run 71. The MUMPs chip was released using the HF release process and sequential curing procedure. The scanning electron micrograph (SEM) images of the various configurations are shown in Fig 4.12.
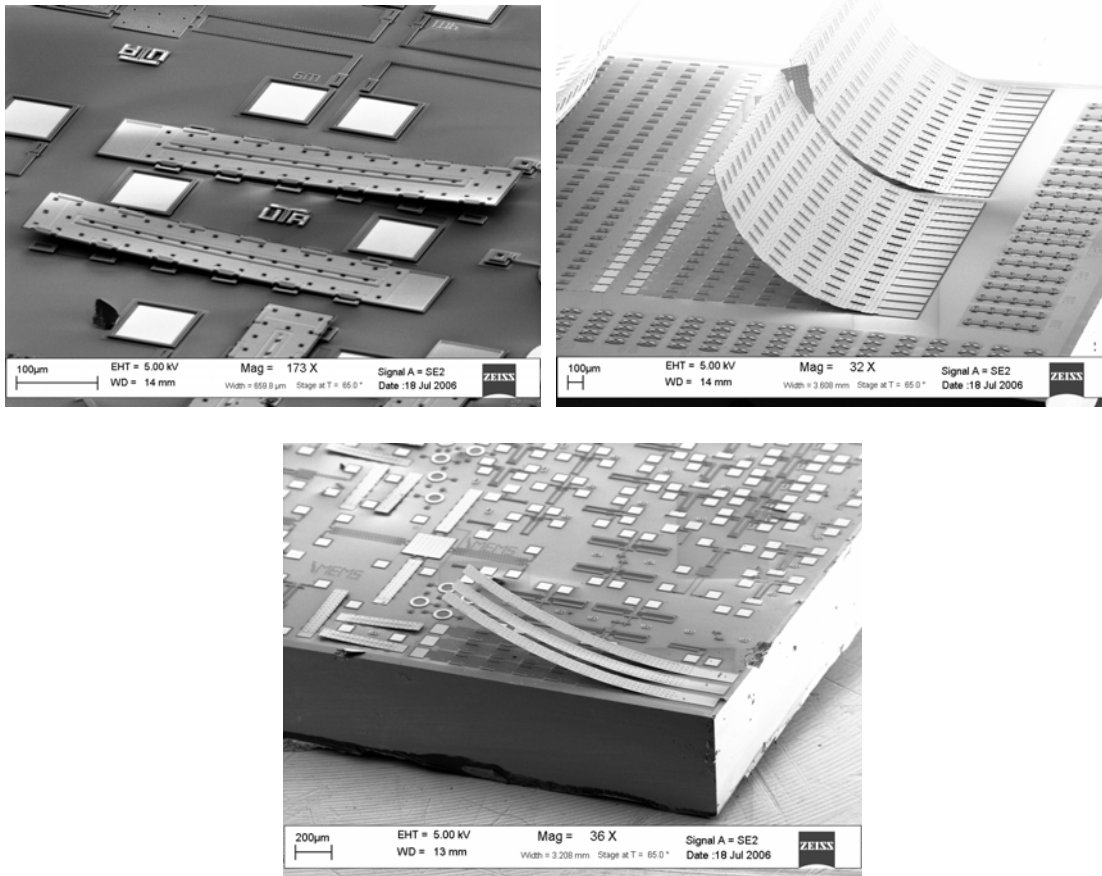
Figure 4.12: SEM images of various configurations of zipper actuators.

The maximum tip deflection of the actuator was determined experimentally using an optical profiler and a reflective microscope. The optical profiler, WYKO NT1100, uses an interferometric microscope to measure the vertical displacement of the actuator. The experimental setup to measure the deflection using the optical profiler is shown in Fig. 4.13.
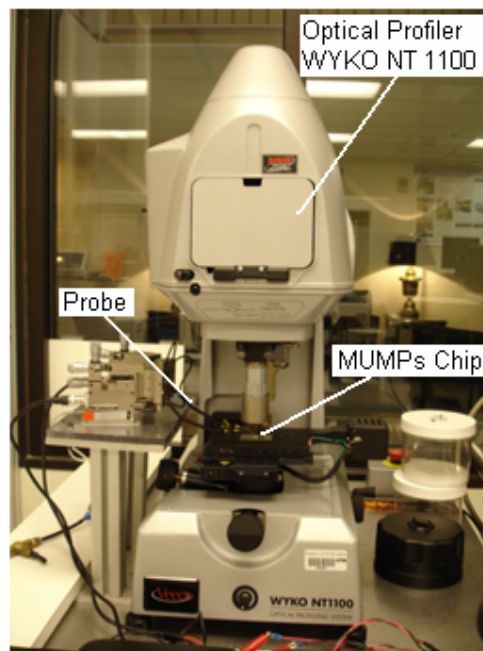
Figure 4.13: Experimental setup to measure deflection of actuator using optical profiler.

The actuation voltage was provided using a voltage amplifier. The electrical current was supplied to the contact pads of actuators by probe. The actuator was dynamically analyzed using the DMEMS option available in the optical profiler. The actuator tip deflections at various input voltages were first measured. The input voltage

was varied from 0 V to 45 V. Fig. 4.14 shows the plot of displacement as a function of

input voltage. It can be seen from the plot that the actuation voltage is low, within 10 V,

and the actuator remains stable for high input voltages.

For the analysis of pull-in voltages, the input voltage was varied from 0 V to 45

V in a step of 0.2 V. The data thus obtained is plotted and is shown in Fig. 4.15. The
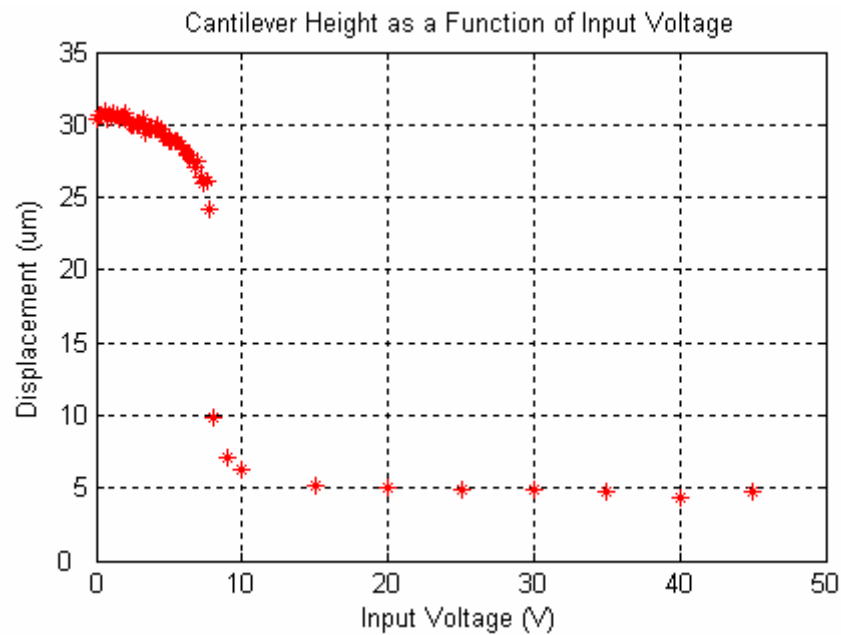
Figure 4.14: Cantilever heights as a function of input voltage.
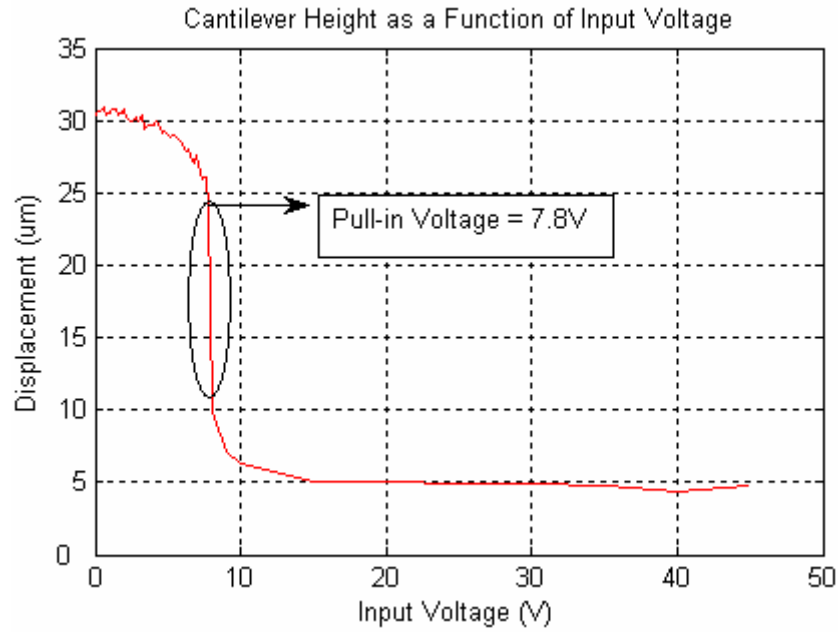
Figure 4.15: Pull-in voltage of the zipper actuator.

height of the cantilever decreases slowly until 7.8 V. The cantilever electrode then collapse to the bottom electrode at 7.8 V. The deflection of the electrode at this point could not be controlled even at a voltage increment of 0.05 V.

The pull-in voltage of 7.8 V is close to the theoretical pull-in voltage range of 4.5 V to 6.7 V. The discrepancy is due to the fact that while doing experiment, the voltage difference due to the resistance of the probe tip has not been considered.

Fig. 4.16 and 4.17 show the profiles of the actuator height along the length and width of the cantilever, respectively. The maximum tip deflection of cantilever is 30.4 μm. The deflection obtained theoretically is 34.334 μm and, 35.58 μm from simulation. Therefore, the errors are within 11.4% and 14.5%, respectively.

69
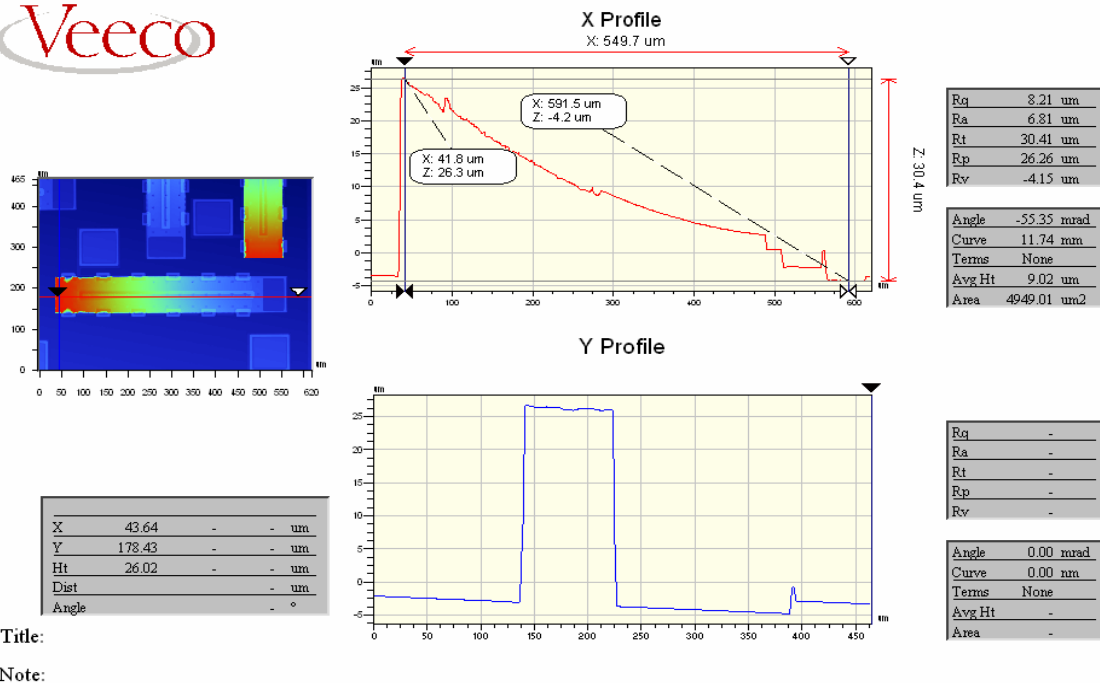
Figure 4.16: Height profile along the length of actuator.
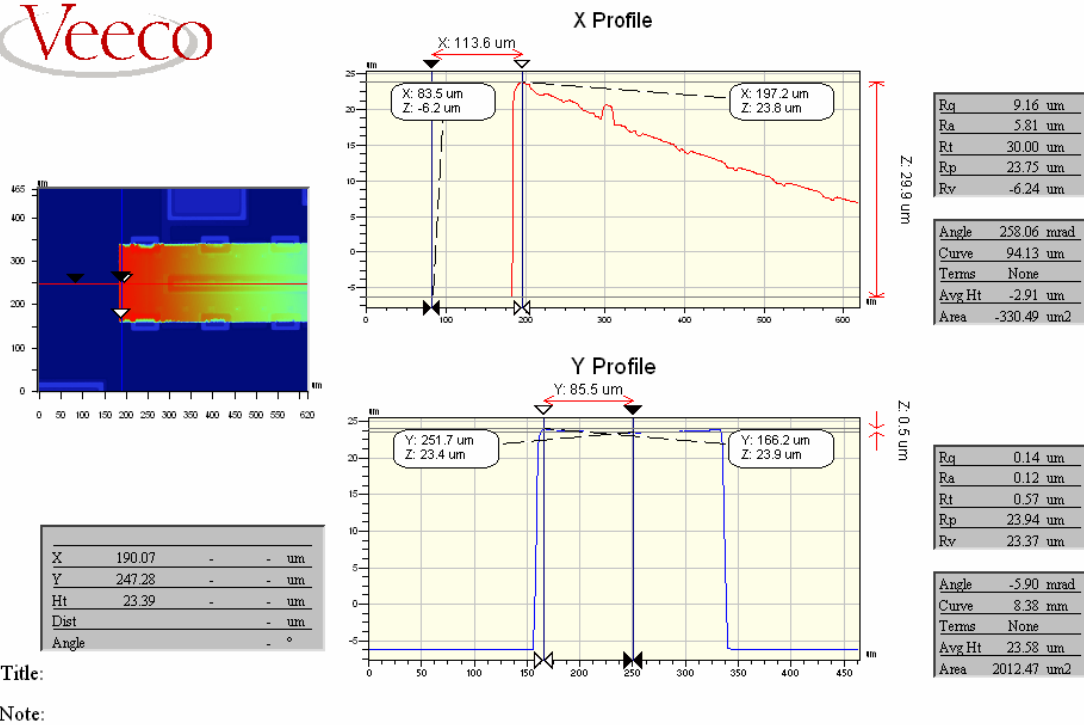
Figure 4.17: Height profile along the width of at free end of the actuator.

70

4.4 Conclusion

In this chapter, a cantilever-type electrostatic zipper actuator was presented. The device was fabricated using multilayer polysilicon process, PolyMUMPs. The static and dynamic characterization was performed. The actuator operates at low voltages. The actuator was characterized in terms of electrostatic force, pull-in voltage, and deflection. A mechanical structure was designed to prevent the electrical shortage of the device without the use of dielectric material. The theoretical and experimental results were verified using the finite element analysis. The actuator can be utilized to design a 2-D optical mirror for use in optical coherence tomography for *in vivo* or *ex vivo* imaging of tissues and organs.

CHAPTER 4

BIDIRECTIONAL VERTICAL THERMAL ACTUATOR

5.1 Introduction

In this chapter, design of a surface micromachined thermal actuator is presented. This actuator can be utilized to design a 2-D optical scanner. Due to the limitation imposed by the body temperature of a thermal actuator, the scanner cannot be used as *in vivo* imaging tool. The scanner can be used for *ex vivo* imaging. The actuation principle of the thermal actuator is based on the asymmetrical thermal expansion of pseudo-bimorph microstructures due to the difference in electrical resistance of two stacked poly-silicon layers. The 3-D imaging is made possible by implementing four such thermal actuators. The thermal actuator is characterized statically and dynamically. The finite element analysis is used to verify the static and dynamic result. The principle of operation, lumped modeling analysis, experimental result and finite element analysis of vertical thermal actuator are addressed in section 5.2.

5.2 Modeling and Analysis of Thermal Actuator

Modeling and analysis of bidirectional vertical thermal actuator is presented in this section. The subjects will be discussed in the order of principle of operation, lumped modeling analysis, experimental results, and finite element analysis.

5.2.1 Principle of Operation

A typical in-plane thermal actuator consists of a hot arm and a cold arm [65]. The hot arm being thinner than the cold arm, has higher electrical resistance, and therefore provides higher temperature when current is applied. Consequently, the hot arm expands more than the cold arm due to difference in thermal expansion resulting in the actuation mechanism. The out-of-plane thermal actuator used in this thesis is similar to the work done by Yen *et al* [66]. This design is the modified design of [67] to provide bi-directional actuation mechanism.
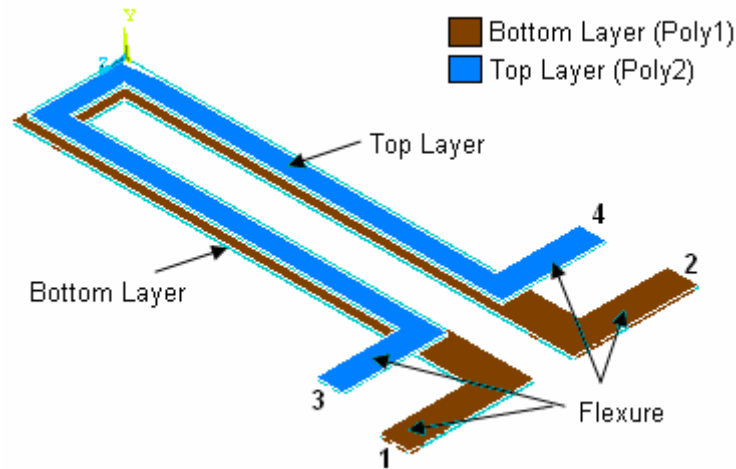
Figure 5.1: 3D view of a bidirectional vertical thermal actuator.

A 3D view of the vertical thermal actuator is shown in Fig. 5.1. The actuator consists of two polysilicon layers connected to each other at one end through via, and anchored to the substrate at the other ends where electrical current can be applied. The actuation principle of the vertical thermal actuator is similar to that in [65] as the

deflection of the actuator tip is due to the difference in thermal expansion of the hot and cold arms. The bi-directional actuation is achieved depending upon the application of electric current on specific electrodes. If the current is applied on the contact pads 1 and 2 in Fig. 5.1, the deflection is upward because the current only pass through the bottom layer which expands due to increase in temperature, whereas if electrical current is applied on contact pads 3 and 4, the deflection is downward. In this thesis, upward deflection has been analyzed by providing electrical currents to the bottom layer i.e. through the contact pads 1 and 2.

5.2.2 Lumped Modeling Analysis

The lumped modeling analysis is based on the work done by [65] and [66]. The analysis is done under the assumption that the heat loss due to radiation is neglected and the analysis is performed as one-dimensional heat transfer problem.

The temperature distribution along the length of top or bottom layer of the actuator is given by

$$T_i = T_s + \frac{B_i}{A_i^2} + C_i e^{A_i x} + C_i' e^{-A_i x} \tag{4.1}$$

where *i* represent number of arms of the top or bottom layer of one dimensional actuator as shown in Fig. 5.2.
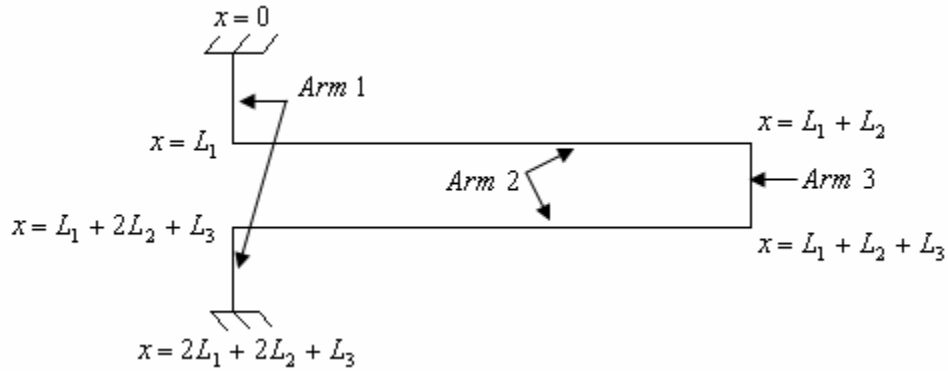
Figure 5.2: One dimensional representation of the thermal actuator [66].

The temperature distribution along the top layer of the thermal actuator can be calculated using Eq. 4.1 and a series of equations given in [66]. The temperature distribution at an input voltage of 5 V is shown in Fig. 5.3. Since a lumped model was
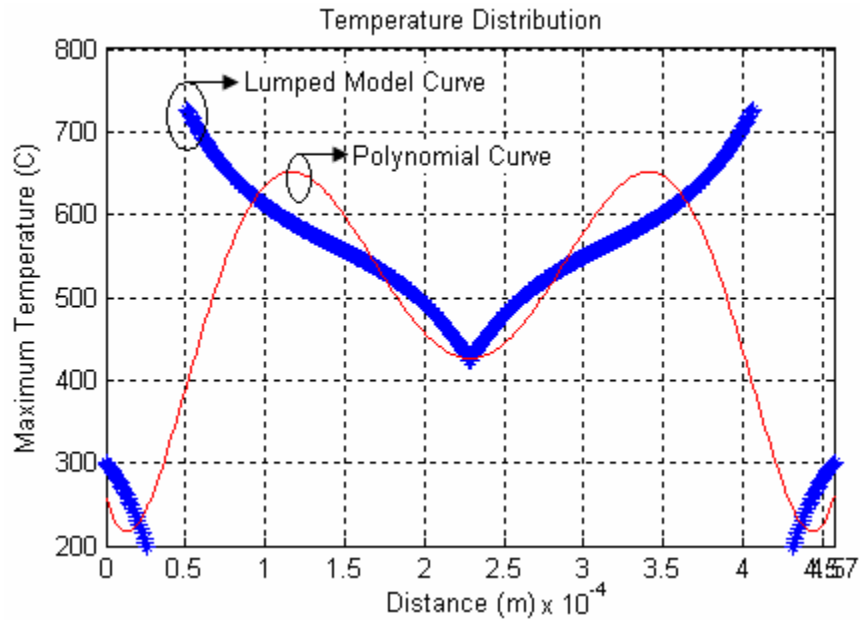
Figure 5.3: Temperature distribution along the top layer of a thermal actuator.

assumed in the analysis, three separate curves are obtained for each of the three arms of the thermal actuator, blue curve in Fig. 5.3. A polynomial curve, shown in red, shows the actual temperature distribution along the top layer. It can be seen from the figure that the temperature distribution is symmetrical about the center line.

Similarly, the actuator tip deflection can be obtained by using linear thermal expansions of the top and bottom layers as an input to the mechanical analysis. Mechanical analysis similar to [66] can be performed to obtain the total tip deflection of the thermal actuator.

Yen *et al* reported a maximum tip deflection of 6 μm at an input voltage of 7 V. This design has been modified and we get the maximum tip deflection of 10.881 μm at an input voltage of 7 V which is approximately 81% increase in total displacement.

The higher deflection of the actuator without significant increase in the actuator body temperature will be verified using the finite element analysis and the experimental results.

5.2.3 Finite Element Analysis

Finite element analysis was used to validate the temperature distribution along the bottom layer and actuator deflection. The actuator model was meshed using a couple field element called "Scalar Tet 98". Three boundary conditions were applied to the model. Thermal boundary condition was applied by keeping the actuator at initial temperature of 27°C. Electrical boundary condition was applied by supplying input voltage. Mechanical boundary condition was applied by applying zero degree of freedom on the contact pads. First, the model provided in [66] was simulated to verify

76

the simulation procedure. The simulation result is shown in Fig. 5.4 at an input voltage of 5 V.
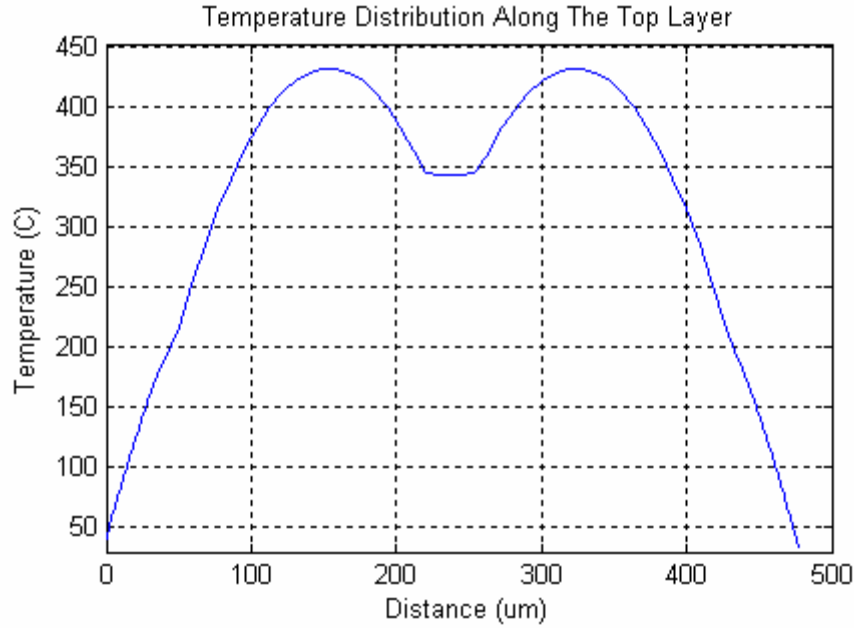
Figure 5.4: Temperature distribution along the top layer of the thermal actuator.

The maximum temperature obtained from simulation is 431.56°C (731.56° K) which is close to the temperature reported on [66] which is 695.36° K. The electrical parameters used for this simulation is obtained from MEMSCap, and is tabulated in Table 5.1. The difference in temperature from [66] and this simulation is due to the difference in electrical parameters. It can be seen from Fig 5.4 that the temperature distribution is symmetrical about the centerline.

Table 5.1: Material properties of Polysilicon.

Material Properties of Polysilicon	Value	Unit
Young's Modulus	$168*10^3$	MPa
Poissons Ratio	0.22	
Thermal Expansion Coefficient	$3.5*10^{-6}$	/°K
Thermal Conductivity	$150*10^6$	pW/µm °K
Resistivity	$2.3*10^{-11}$	Ω-µm

Similar procedure is carried out to obtain the temperature distribution for the modified design at input voltage of 5V. Fig 5.5 (a) and (b), and 5.6 (a) and (b) show the temperature distribution along the bottom layer of various configurations of thermal actuators. Fig 5.7 delineates the plot of maximum temperature as a function of input voltage. It can be seen from the plot that there is no significant increase in temperature with decrease in the flexure length of the top layer. Fig. 5.8 delineates the plot of maximum displacement as a function of input voltage. It can be seen from the plot that the actuator with flexure length of 20 µm has maximum displacement of 10.881 µm at an input voltage of 7 V which is 4.8 µm (81%) greater than the displacement reported by [66].
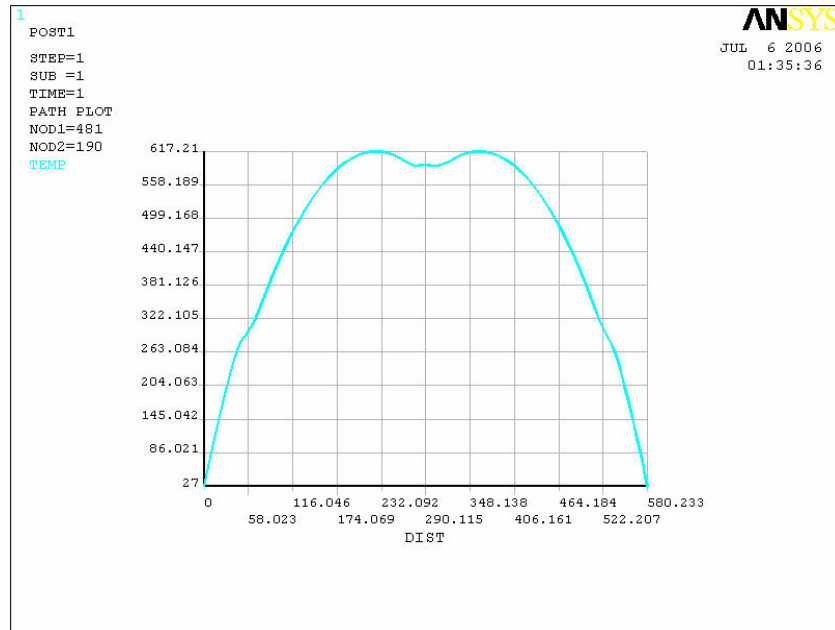
(a)
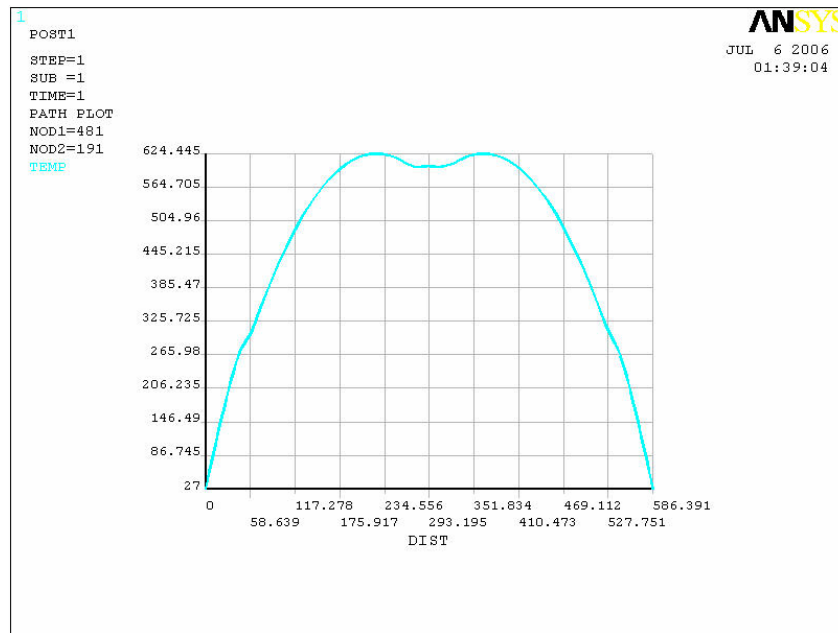
(b)

Figure 5.5: Temperature distribution along the bottom layer of actuators with flexure length of (a) 20 µm, and (b) 30 µm.
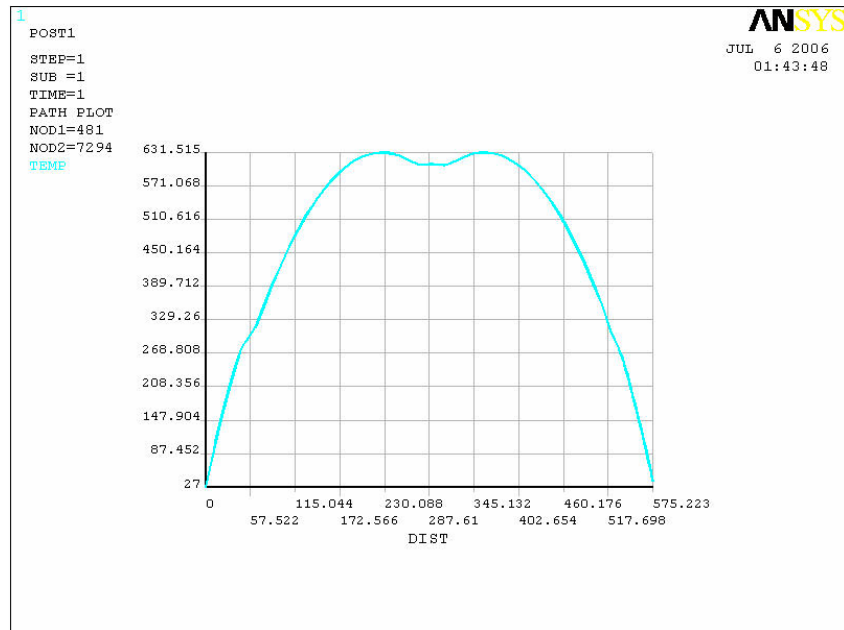
(a)
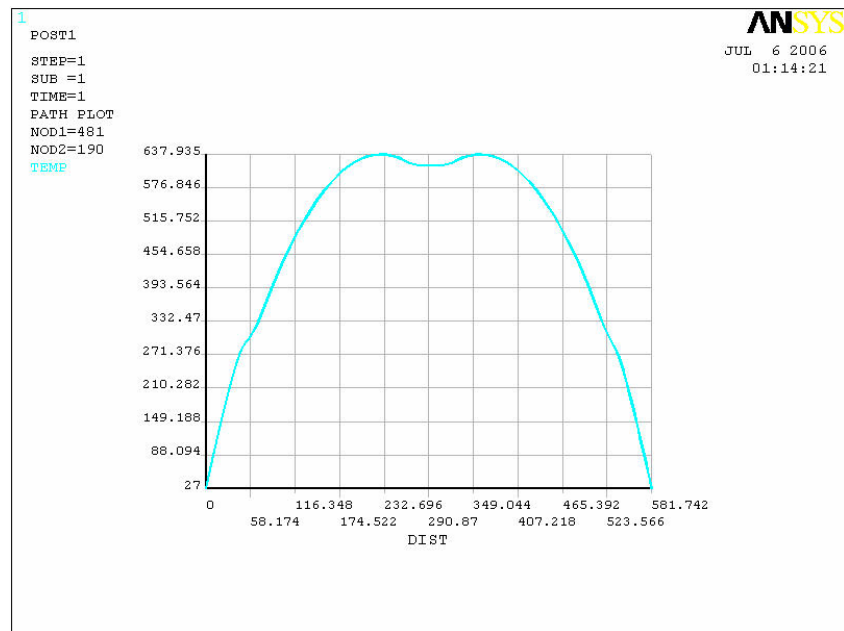
(b)

Figure 5.6: Temperature distribution along the bottom layer of actuators with flexure length of (a) 40 µm, and (b) 50 µm.
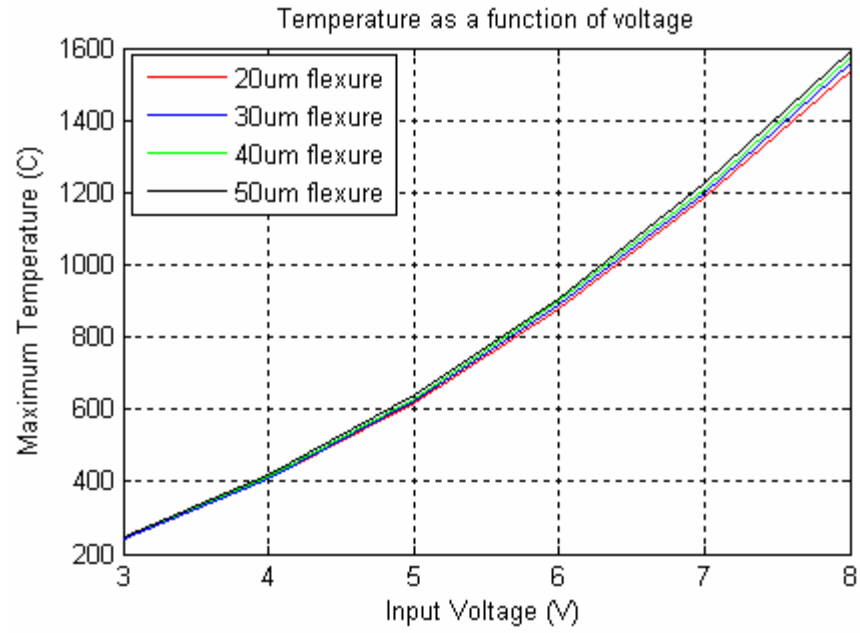
Figure 5.7: Maximum temperature as a function of an input voltage.
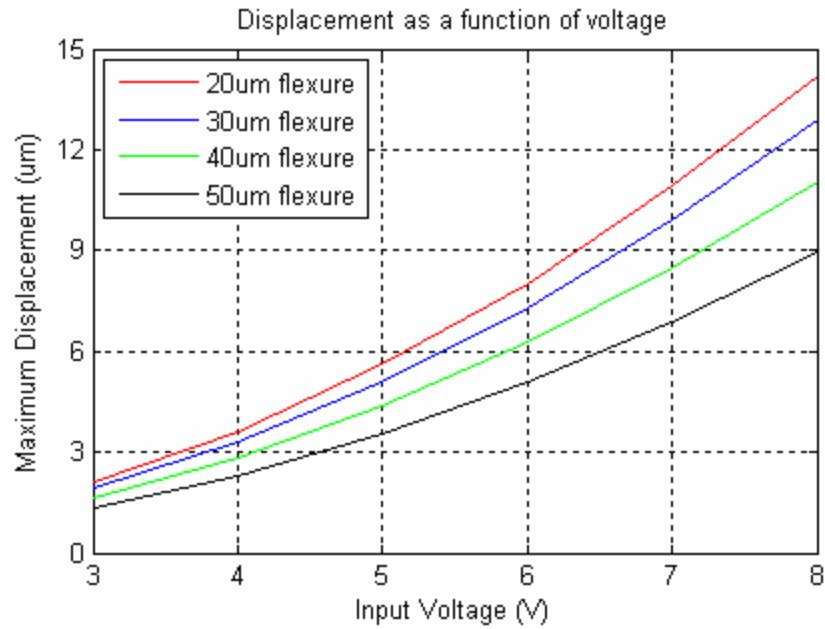
Figure 5.8: Maximum displacement as a function of an input voltage.
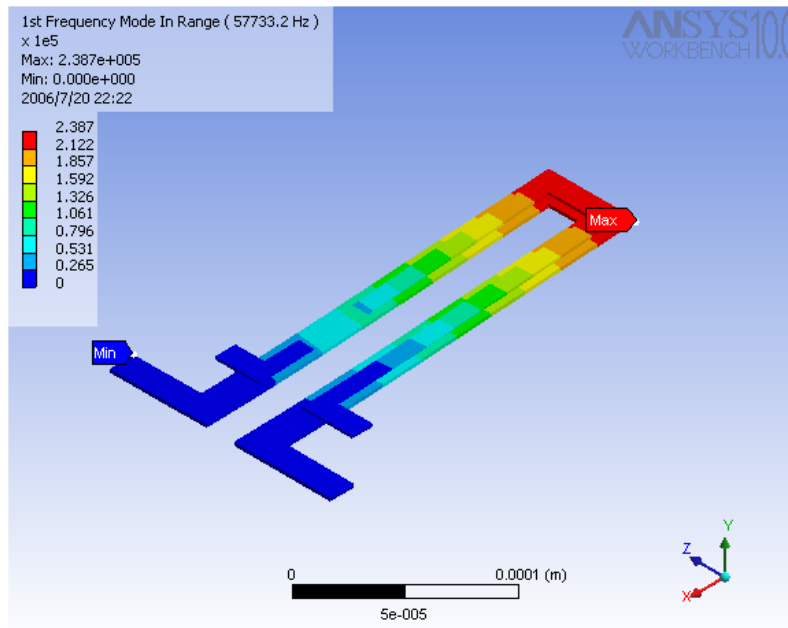
(a)
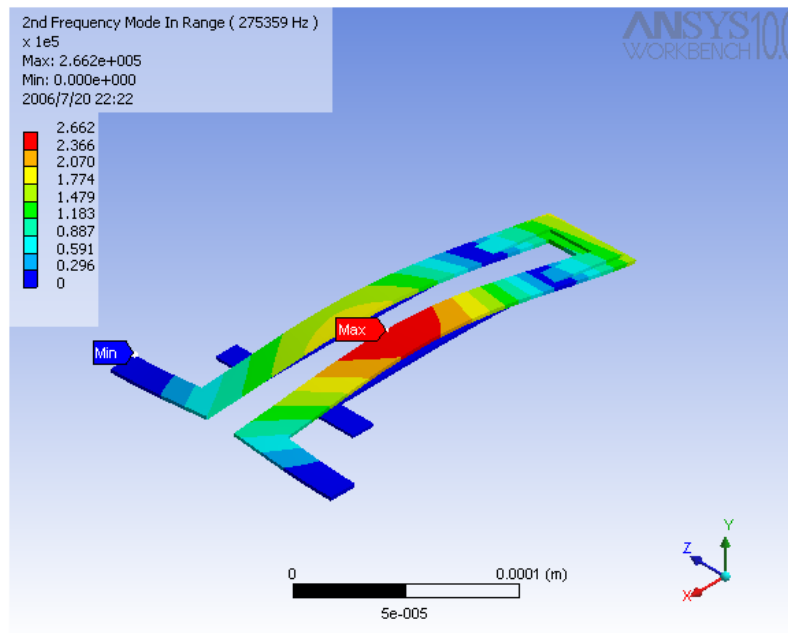
(b)

Figure 5.9: A mechanical resonant frequency of a thermal actuator. (a) first mode, and (b) second mode.

Modal analysis was performed to obtain the resonant frequency of a thermal actuator. The first and second mode of a mechanical resonant frequency is 7.14 KHz and 44.734 KHz, respectively. The simulation result is shown in Fig. 5.9.

5.2.4 Experimental Result

Various configuration of vertical thermal actuator were fabricated using the MUMPs process, run 71. The MUMPs chip was released using the HF release process. The scanning electron micrograph (SEM) images of the various configurations are shown in Fig.5.10.
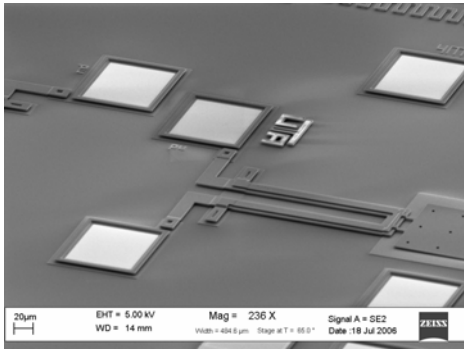
<div align="center">(a)</div>
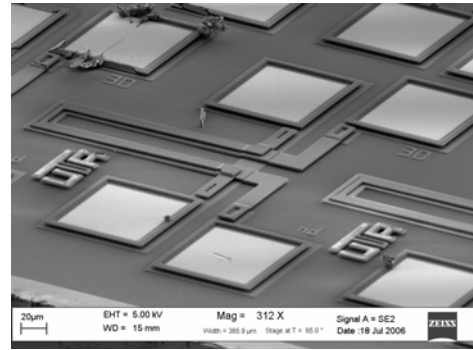
<div align="center">(b)</div>
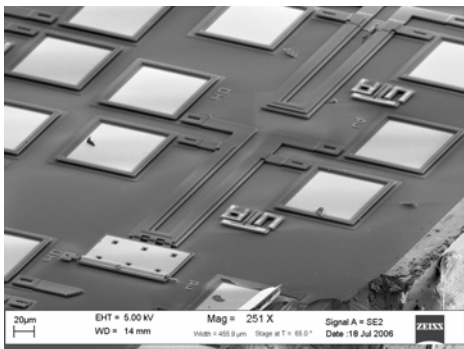
<div align="center">(c)</div>
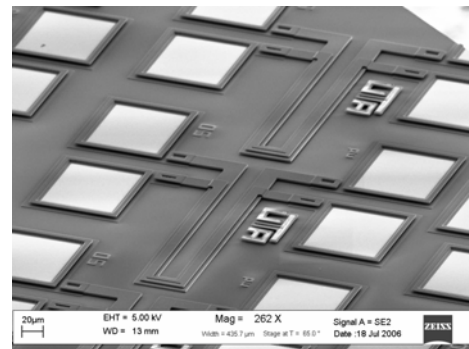
<div align="center">(d)</div>

Figure 5.10: Scanning electron micrograph of vertical thermal actuators with flexure length of (a) 20 μm, (b) 30 μm, (c) 40 μm, and (d) 50 μm.

The maximum tip deflection of the actuator was determined experimentally using the optical profiler and a reflective microscope. The optical profiler, WYKO NT1100, uses interferometric microscope to measure the vertical displacement of the actuator. The experimental setup to measure the deflection is shown in Fig. 4.13.

The actuation voltage was provided using the current amplifier. The electrical current was supplied to the contact pads of actuators by probe. The actuator was dynamically analyzed using the DMEMS option available in optical profiler. For the measurement, a square wave with an amplitude of 7 V and 20% duty cycle was supplied, and then the optical reading were taken at every 10° phase difference. The experimental data is plotted and curve fitted to measure the maximum displacement. Maximum displacement as a function of phase angle is plotted in Fig 5.11, 5.12, 5.13, and 5.14.

It can be seen from the Fig 5.10 that there is a good agreement between the measured actuator displacement and the finite element analysis.
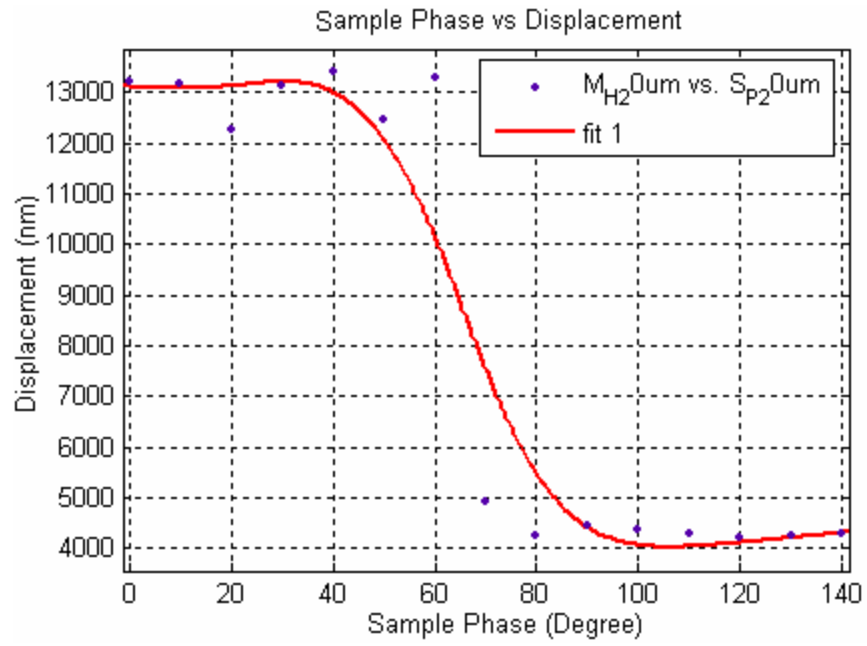
Figure 5.11: Maximum displacement as a function of phase angle for actuators with flexure length of 20 µm.

(b)
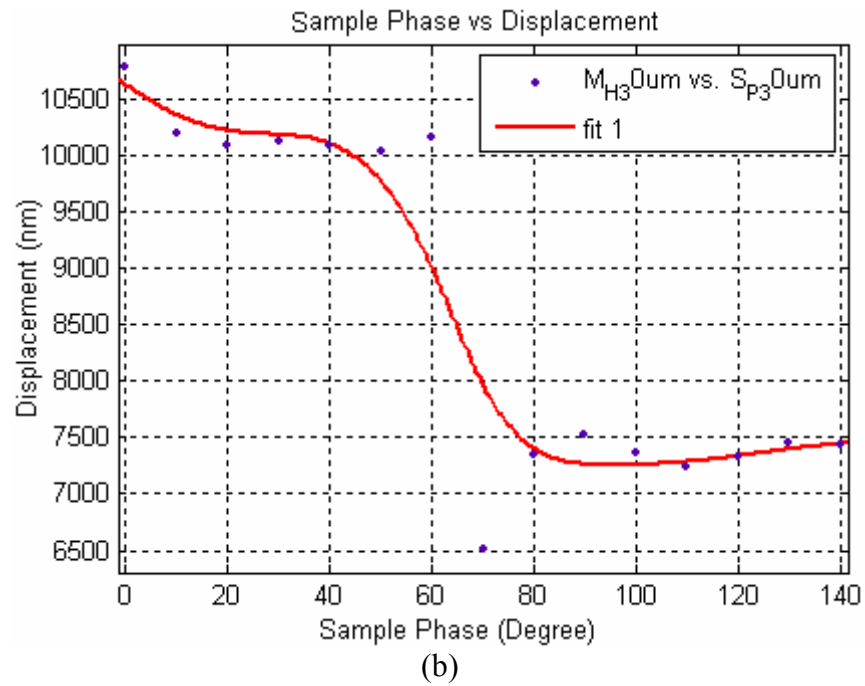
Figure 5.12: Maximum displacement as a function of phase angle for actuators with flexure length of 30 µm.
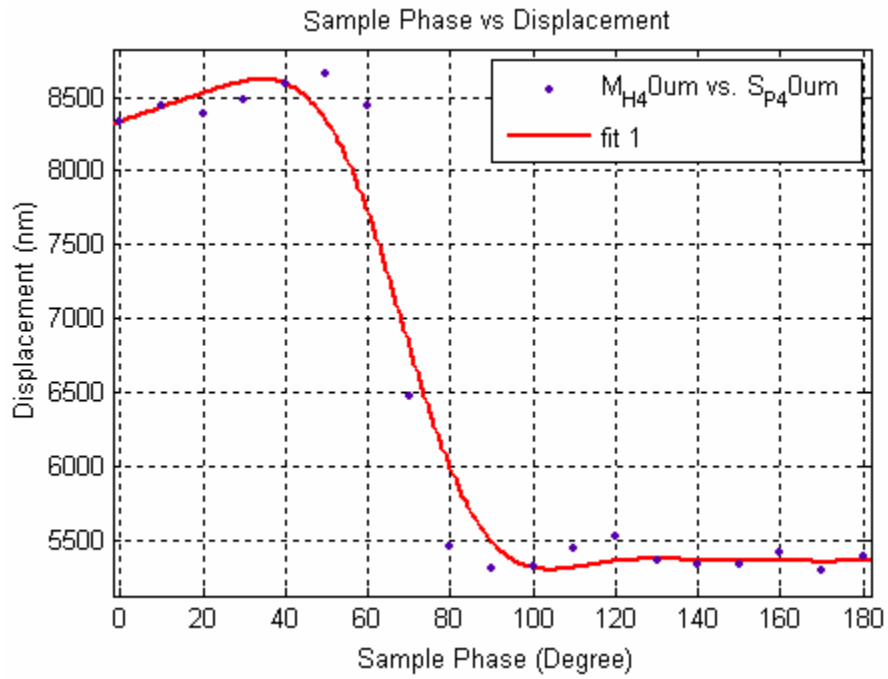
Figure 5.13: Maximum displacement as a function of phase angle for actuators with flexure length of 40 μm.
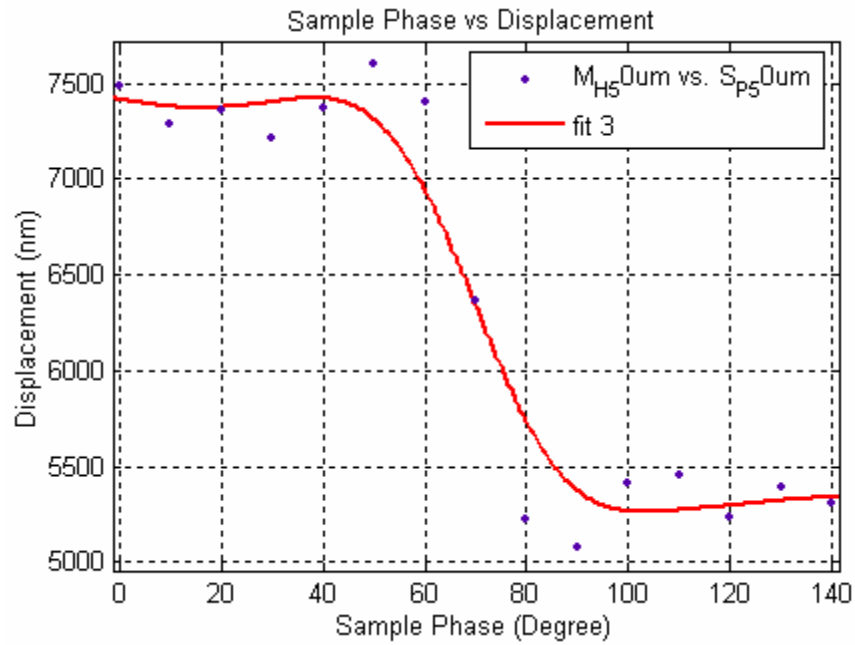
Figure 5.14: Maximum displacement as a function of phase angle for actuators with flexure length of 20 μm.

5.3 Conclusions

In this chapter, a bidirectional vertical thermal actuator was presented. The device was fabricated using multilayer polysilicon process, PolyMUMPs. The actuator was statically and dynamically characterized using a optical profiler. The actuator was modified to achieve higher displacement without significant increase in the body temperature. The theoretical and experimental results were verified using finite element analysis. The actuator can be utilized to design a 2-D optical mirror for use in optical coherence tomography for *ex vivo* imaging of tissues and organs.

CHAPRTER 6

CONCLUSIONS

A 1-D fiber optic scanner based on electromagnetic actuation was introduced. A brush coating technique was implemented to coat a thin ferromagnetic material on single-mode optical fibers. The static and dynamic characterization of the scanner was performed. The theoretical and experimental results were verified using the finite element analysis. A cantilever-type electrostatic zipper actuator and a bidirectional vertical thermal actuator was presented. The static and dynamic characterization was performed. The theoretical and experimental results were verified using the finite element analysis.

APPENDIX A

MATLAB CODE

```
% STATIC DISPLACEMENT

 % Theoritical Calculation

close all

clear all

 Data1=load('Static_Theo_Final.txt');

% First column=current(A)

% Second collumn=Ho (A/m)

% Third column=Gradient of magnetic field

% Fourth column=Dipole moment M

% Fifth column= X1 (um) for 4.2 cm

% Sixth column= X2 (um) for 4.2 cm

% Seventh column= X1 (um) for 5.2 cm

% Eighth column= X2 (um) for 5.2 cm

% Nineth column= X1 (um) for 3.2 cm

% Tenth column= X2 (um) for 3.2 cm

 I=Data1(:,1);

Ho=Data1(:,2);

Grad_H=Data1(:,3);

M_Ho=Data1(:,4);

X1_42cm=Data1(:,5);                              % Data of 4.2 cm fiber

X2_42cm=Data1(:,6);

X1_52cm=Data1(:,7);                              % Data of 5.2 cm fiber
```

```
X2_52cm=Data1(:,8);

X1_32cm=Data1(:,9);                              % Data of 3.2 cm fiber

X2_32cm=Data1(:,10);

muo=pi*4e-7;                                     % Permeability of air

E=72.39e9;                                       % Young's Modulus of fiber

r=62.5e-6;                                       % Radius of fiber

rfc_42cm=125e-6;                                 % Radius of fiber+gel coating

rfc_52cm=110e-6;                                 % Radius of fiber+gel coating

rfc_32cm=100e-6;                                 % Radius of fiber+gel coating

l_coat_42=.6e-2;                                 % Length of Ni coating on 4.2cm

l_coat_52=.6e-2;                                 % Length of Ni coating on 5.2cm

l_coat_32=.6e-2;                                 % Length of Ni coating on 3.2cm

l_42cm=4.2e-2;                                    % Length of fiber

l_52cm=5.2e-2;                                   % Length of fiber

l_32cm=3.2e-2;                                   % Length of fiber

v_42cm=(pi*(rfc_42cm^2)-pi*(r^2))*l_coat_42;     % volume of coating

V_42cm=0.3*v_42cm;                               % Considering 30% nickel

v_52cm=(pi*(rfc_52cm^2)-pi*(r^2))*l_coat_52;     % volume of coating

V_52cm=0.3*v_52cm;                               % Considering 30% nickel


v_32cm=(pi*(rfc_32cm^2)-pi*(r^2))*l_coat_32;     % volume of coating

V_32cm=0.3*v_32cm;                               % Considering 30% nickel
```

```matlab
a=0.75e-2;

b_42cm=3.45e-2;

b_52cm=4.45e-2;

b_32cm=2.45e-2;

Lx=12                                        % PSD active area in mm

% Circular area moment of inertia

I=(pi*r^4)/4;

% Linear spring constant 4.2 cm

K_42cm=1/((b_42cm^3/(3*E*I))+(a^3/(2*E*I)));

% Linear spring constant 5.2 cm

K_52cm=1/((b_52cm^3/(3*E*I))+(a^3/(2*E*I)));

% Linear spring constant 3.2 cm

K_32cm=1/((b_32cm^3/(3*E*I))+(a^3/(2*E*I)));;

% Linear diflection of fiber

Fmag_42cm=muo*V_42cm*(M_Ho.*Grad_H);

% Linear diflection of fiber

Fmag_52cm=muo*V_52cm*(M_Ho.*Grad_H);

% Linear diflection of fiber

Fmag_32cm=muo*V_32cm*(M_Ho.*Grad_H);

 D_42cm=Fmag_42cm./K_42cm;                   % In meter

d_42cm=D_42cm*1000;                          % In mm

 D_52cm=Fmag_52cm./K_52cm;                   % In meter
```

```matlab
d_52cm=D_52cm*1000;                    % In mm

D_32cm=Fmag_32cm./K_32cm;              % In meter

d_32cm=D_32cm*1000;                    % In mm

% Experimental Calculation

 X_42cm=X2_42cm.*Lx;

Io_42cm=X1_42cm+X2_42cm;

x_42cm=X_42cm./Io_42cm;

 dis_42cm=x_42cm(1)-x_42cm;            % Displacement in mm

 X_52cm=X2_52cm.*Lx;

Io_52cm=X1_52cm+X2_52cm;

x_52cm=X_52cm./Io_52cm;

dis_52cm=x_52cm(1)-x_52cm;            % Displacement in mm

 X_32cm=X2_32cm.*Lx;

Io_32cm=X1_32cm+X2_32cm;

x_32cm=X_32cm./Io_32cm;

dis_32cm=x_32cm(1)-x_32cm;            % Displacement in mm

plot(Ho,d_42cm,'*')                   % Theoritical plot 4.2cm

hold on

plot(Ho,dis_42cm,'^')                 % Experimental plot 4.2 cm

title('Static Displacement');

xlabel('H(A/m)');

ylabel('Displacement (mm)');
```

```matlab
legend('Theoretical result for 4.2cm','Theoretical result for 4.2cm');

grid on;

figure

plot(Ho,d_52cm,'s')                          % Theoritical plot 5.2cm

hold on

plot(Ho,dis_52cm,'x')                        % Theoritical plot 5.2cm

title('Static Displacement');

xlabel('H(A/m)');

ylabel('Displacement (mm)');

legend('Theoretical result for 5.2cm','Experimental result for 5.2 cm');

grid on;

figure

plot(Ho,d_32cm,'s')                          % Theoritical plot 5.2cm

hold on

plot(Ho,dis_32cm,'x')                        % Theoritical plot 5.2cm

title('Static Displacement');

xlabel('H(A/m)');

ylabel('Displacement (mm)');

legend('Theoretical result for 3.2cm','Experimental result for 3.2 cm');

grid on;

figure

% DYNAMIC DIAPLACEMENT
```

```matlab
Data2=load('Dynamic.txt');

% First collumn=Input frequency (Hz) for 4.2cm

% Second column=Output frequency (Hz) for 4.2cm

% Third column=X1_42cm_min (mV) for 4.2 cm

% Fourth column=X1_42cm_max (mV) for 4.2 cm

% Fifth column=X2_42cm_min (mV) for 4.2 cm

% Sixth column=X2_42cm_max (mV) for 4.2 cm

% Seventh column=Input frequency (Hz) for 5.2cm......

Input_f_42cm=Data2(:,1);                    % Data of 4.2 cm fiber

Output_f_42cm=Data2(:,2);

X1_42cm_min=Data2(:,3);

X1_42cm_max=Data2(:,4);

X2_42cm_min=Data2(:,5);

X2_42cm_max=Data2(:,6);

Input_f_52cm=Data2(:,7);                    % Data of 5.2 cm fiber

Output_f_52cm=Data2(:,8);

X1_52cm_min=Data2(:,9);

X1_52cm_max=Data2(:,10);

X2_52cm_min=Data2(:,11);

X2_52cm_max=Data2(:,12);

Xd_42cm_1=X2_42cm_max.*Lx;

Ido_42cm_1=X2_42cm_max+X1_42cm_min;
```

```matlab
xd_42cm_1=Xd_42cm_1./Ido_42cm_1;


Xd_42cm_2=X2_52cm_min.*Lx;

Ido_42cm_2=X1_42cm_max+X2_52cm_min;

xd_42cm_2=Xd_42cm_2./Ido_42cm_2;

Xd_42cm=xd_42cm_1-xd_42cm_2;              % Displacement in mm for 4.2 cm

Xd_52cm_1=X2_52cm_max.*Lx;

Ido_52cm_1=X2_52cm_max+X1_52cm_min;

xd_52cm_1=Xd_52cm_1./Ido_52cm_1;

Xd_52cm_2=X2_52cm_min.*Lx;

Ido_52cm_2=X1_52cm_max+X2_52cm_min;

xd_52cm_2=Xd_52cm_2./Ido_52cm_2;

Xd_52cm=xd_52cm_1-xd_52cm_2;              % Displacement in mm for 5.2 cm

plot(Input_f_42cm,Xd_42cm,'*');

hold on

plot(Input_f_52cm,Xd_52cm,'x');

legend('Experimental result of 4.2cm','Experimental result of 5.2cm');

title('Dynamic Displacement');

xlabel('Input Frequency (Hz)');

ylabel('Displacement (mm)');

grid on;
```

REFERENCES

[1] D. Huang, E. A. Swanson, C. P. Lin, J. S. Schuman, W. G. Stinson, W. Chang, M. R. Hee, T. Flotte, K. Gregory, C. A. Puliafito, and J. G. Fujimoto. (1991). Optical coherence tomography. <u>Science</u>, 254:1178-1181.

[2] W. Drexler, U. Morgner, F. X. Kartner, C. Pitris, S. A. Boppart, X. D. Li, E. P. Ippen, and J. G. Fujimoto. (1999). *In vivo* ultrahigh-resolution optical coherence tomography. <u>Optics Letters</u>, 24:1221-1223.

[3] R. C. Youngquist, S. Carr, and D. E. N. Davies. (1987). Optical coherence-domain reflectometry: A new optical evaluation technique. <u>Optics Letters</u>, 12:158-160.

[4] A. F. Fercher, K. Mengedoht, and W. Werner. (1988) Eye-length measurement by interferometry with partially coherent-light. <u>Optics Letters</u>, 13:186-188.

[5] A. M. Rollins, R. Ung-arunyawee, A. Chak, R. C. K. Wong, K. Kobayashi, and M. V. Sivak. (1999). Real-time *in vivo* imaging of human gastrointestinal ultrastructure by use of endoscopic optical coherence tomography with a novel efficient interferometer design. <u>Optics Letters</u>, 24:1358-1360.

[6] B. Cense, T. C. Chen, B. H. Park, M. C. Pierce, and J. F. Boer. (2002). In vivo depth-resolved birefringence measurement of the human retinal nerve fiber layer by polarization-sensitive optical coherence tomography. <u>Optics Letters</u>, 27:1610-1612.

[7] V. J. Srinivasan, M. Wojtkowski, and J. G. Fujimoto. (2006). *In vivo* measurement of retinal physiology with high-speed ultrahigh-resolution optical coherence tomography. <u>Optics Letters</u>, 31:2308-2310.

[8] A. F. Fercher, C. K. Hitzenberger, W. Drexelr, G. Kamp, and H. Sattmann. (1993). *In vivo* optical coherence tomography. <u>American Journal of Ophthalmology</u>, 116:113-114.

[9] E. A. Swanson, J. A. Izatt, M. R. Hee, D. Huang, C. P. Lin, J. S. Schuman, C. A. Puliafito, and J. G. Fujimoto. (1993). *In vivo* retinal imaging by optical coherence tomography. <u>Oprics Letters</u>, 18:1864-1866.

[10] C. K. Patel. (2006). Optical coherence tomography in the management of acute retinopathy of prematurity. <u>American Journal of Ophthalmogy</u>, 3:582-584.

[11] J. A. Izatt, M. D. Kulkarni, H. W. Wang, K. Kobayashi, and V. Sivak. (1996). Optical coherence tomography and microscopy in gastrointestinal tissues. <u>IEEE Journal of Selected Topics in Quantum Electronics</u>, 2(4):1017-1028.

[12] C. Pitris, M. E. Brezinski, B. E. Bouma, G. J. Tearney, J. F. Southern, and J. G. Fujimoto. (1998). High-resolution imaging of the upper respiratory tract with optical coherence tomography: A feasibility study. <u>American Journal of Respiratory and Critical Care Medicine</u>, 157:1640-1644.

[13] G. J. Tearney, M. E. Brezinski, J. F. Southern, B. E. Bouma, S. A. Boppart, and J. G. Fujimoto. (1998). Optical biopsy in human pancreatobiliary tissue using optical coherence tomography. <u>Digestive Diseases and Sciences</u>, 43:1193-1199.

[14] S. A. Boppart, B. E. Bouma, C. Pitris, J. F. Southern, M. E. Brezinski, and J. G. Fujimoto. (1998). Intraoperative assessment of microsurgery with three-dimensional optical coherence tomography. <u>Radiology</u>, 208:81-86.

[15] I. Hartl, X. D. Li, C. Chudoba, R. K. Ghanta, T. H. Ko, J. G. Fujimoto, J. K. Ranka, and R. S. Windeler. (2001). Ultrahigh-resolution optical coherence tomography using continuum generation in an air-silica microstructure optical fiber. <u>Optics Letters</u>, 26:608-610.

[16] A. Dubois, G. Moneron, and C. Boccara. (2006). Thermal-light full-field optical coherence tomography in the 1.2 μm wavelength region. <u>Optics Communications</u>, xxx:xxx-xxx.

[17] G. J. Tearney, B. E. Bouma, and J. G. Fujimoto. (1997). High-speed phase- and group-delay scanning with a grating-based phase control delay time. <u>Optics Letters</u>, 22:1811-1813.

[18] Y. Watanabe, K. Yamada, and M. Sato. (2006). In vivo non-mechanical scanning grating-generated optical coherence tomography using an InGaAs digital camera. <u>Optics Communications</u>, 261:376-380.

[19] M. Ikeda, H. Goto, H. Totani, M. Sakata, and T. Yada. (1997). Two-dimensional miniature optical-scanning sensor with silicon micro-machined scanning mirror. <u>SPIE</u> Volume 3008.

[20] G. -D. J. Su, H. Toshiyoshi, and M. C. Wu. (June 2001). Surface-micromachined 2-D optical scanners with high-performance single-crystalline silicon micromirrors. IEEE Photonics Technology Letters, 13 (6), 606-608.

[21] W. Piyawattanametha, P. R. Patterson, D. Hah, H. Toshiyoshi, and M. C. Wu. (December 2005). Surface- and bulk-micromachined two-dimensional scanner driven by angular vertical comb actuators. Journal of Microelectromechanical systems, 14 (6), 1329-1337.

[22] W. Jung, J. Zhang, L. Wang, P. W. Smith, Z. Chen, D. T. McCormick, and N. C. Tien. (2005). Three-dimensional optical coherence tomography employing a 2-axis microelectromechanical scanning mirror. IEEE Journal of Selected Topics in Quantom Electronics, 11 (4), 806-810.

[23] R. A. Conant, J. Nee, M. Hart, O. Solgaard, K. Y. Lou, and R. S. Muller. (1999). Robustness and reliability of micromachined scanning mirrors. MOEMS.

[24] M. H. Kiang, O. Solgaard, K. Y. Lau, and R. S. Muller. (1998). Polysilicon optical microscanners for laser scanning siaplays. Sensors and Actuators, A70:195-199.

[25] S. P. Fang, and H. F. Taylor. (1994). High-performance single-mode fiber-optic switch. Optics Letters, 19:1204-1206.

[26] Shi-Sheng Lee, Ed Motamedi, and Ming C. Wu. (1997). Surface-micromachined free-Space Fiber Optic Switches With Integrated Microactuators for Optical Fiber Communication Systems. TRANSDUCERS'97 1997 International Conference on Solid-State Sensors and Actuators, Chicago, June 16-19.

[27] I. R. Matias, M. Lopez-Amo, F. Montero, C. Fernandez-Valdivielso, F. J. Arregui, and C. Bariain. (January 2001). Low-cost optical amplitude modulator based on a tapered single-mode optical fiber. <u>Applied Optics</u>, Vol. 40, No.2.

[28] S.A. Boppart, B.E. Bouma, C. Pitris, G.J. Tearney, and J.G. Fujimoto. (November 1997). Forward-imaging instruments for optical coherence tomography. <u>Optics Letters</u>, Vol. 22, No. 21.

[29] Nelson RW, Krone JR, and Jansson O. (Nov 1997). Surface plasmon resonace biomolecular interaction analysis mass spectrometry. <u>Anal Chem</u>, 69(21):4369-74.

[30] Miroslav Sedlar, Vlastimil Matejec, and Ivan Paulicka. (2000). Optical fibre magnetic field sensors using ceramic magnetostrictive jackets. <u>Sensors and Actuators</u>, 84: 297-302.

[31] R.S. Popovic, J.A. Flanagan, and P.A. Besse. (1996). The future of magnetic sensors. <u>Sensor and Actuators</u>, A56:39-55.

[32] Franz Keplinger, Samuel Kvasnica, Artur Jachimowicz, Franz Kohl, Johannes Steurer, and Hans Hauser. (2004). Lorentz force based magnetic field sensor with optical readout, <u>Sensors and Actuators</u>, A 110:112-118.

[33] S.P. Fang and H.F. Taylor. (1994). High-performance single-mode fiber-optic switch. Optics Letters, Vol. 19, No. 15.

[34] Shi-Sheng Lee, Ed Motamedi, and Ming C. Wu. (1997). Surface-micromachined free-space fiber optic switches with integrated microactuators for optical fiber

communication systems. <u>TRANSDUCERS'97 1997 International Conference on Solid-State Sensors and Actuators</u>, Chicago, June 16-19.

[35] Mark Herding, Franz Richardt, and Peter Woias. (2003). A novel approach to low-cost optical fiber switches. <u>IEEE</u>.

[36] Martin Hoffmann, Peter Kopka, Edgar Voges. (1999). Bistable micromechanical fiber-optic switches on silicon with thermal actuators. <u>Sensors and Actuators</u>, 78:28-35.

[37] Kevin R. Cochran, Lawrence Fan, Don L. DeVoe. (October 2004). High-power optical microswitch based on direct fiber aActuation. <u>Sensor and Actuators</u>.

[38] Shinji Nagaoka. (January/February 1999). Compact latching-type single-mode-fiber switches fabricated by a fiber-micromachining technique and their practical applications. <u>IEEE Journal of Selected Topics in Quantum Electronics</u>, Vol. 5, No. 1.

[39] Jonathan J. Bernstein, William P. Taylor, John D. Brazzle, Christopher J. Corcoran, Gregory Kirkos, Jefferson E. Odhner, Ajay Pareek, Marc Waelti, and Marvin Zai. (June 2004). Electromagnetically actuated mirror arrays for use in 3-D optical swtiching applications. <u>Journal of Microelectromechanical Systems</u>, Vol. 13, No. 3.

[40] Merritt N. Deeter. (April 1995). High sensitivity fiber-optic magnetic field sensors based on iron garnets. <u>IEEE Transactions on Instrumentation and Measurement</u>, Vol. 44, No. 2.

[41] http://usa.hamamatsu.com/assets/pdf/catsandguides/Psd.pdf

[42] J. Topfer, and V. Christoph. (2004). Multi-pole magnetization of NdFeB sintered magnets and thick films for magnetic micro-actuators. <u>Sensors and Actuators.</u> A113:257-263.

[43] M. Sendoh, Ishiyama, and K.-I. Arai. (September 2003). Fabrication of magnetic actuator for use in a capsule endoscope. <u>IEEE Transactions on Magnetics</u>, Vol. 39, No. 5.

[44] P. N. Singh, P. K. Jha. (1980). Elemantary Mechanics of Solids, John and Wiley & Sons, Inc.

[45] R. E. Rosensweig, (1985). Ferrohydrodynamics, Cambridge University Press.

[46] J. P. Den Hartog, (1985). Mechanical Vibrations, Dover Publications, Inc.

[47] Yun-Ho Jang, and Yong-Kweon Kim. (2003). Design, fabrication and characterization of an electromagnetically actuated addressable out-of-plane micromirror array for vertical optical source applications. <u>Journal of Micromechanics and Microengineering</u>, 13:853-863.

[48] Mitsunori Saito, Kaoru Nakajima, and Mitsunobu Shishido. (March 2002). Polymer coating on infrared silver halide fiber for photodarkening protection. <u>Journal of Lightwave Technology</u>, Vol. 20, No. 3.

[49] Yoko Okano, and Yasuo Hirabayashi. (January/February 2002). Magnetically actuated micromirror and measurement system for motion characteristics using specular reflection. <u>IEEE Journal on Selected Topics in Quantum Electronics</u>, Vol. 8, No. 1.

[50] Miroslav Sedlar, Vlastimil Matejec, and Ivan Paulicka. (2000). Optical fiber magnetic field sensor using ceramic magnetostrictive jackets. Sensors and Actuators, 84:297-302.

[51] Marc J. Madau, Fundamentals of Micro-fabrication: The Science of Miaturization, Second Edition, CRC Press.

[52] Hans P. Hu, PhD Candidate, UTA.

[53] J. Li, M. P. Brenner, J. H. Lang, A. H. Slocum, and R. Struempler. (June 2003). DRIE-Fabricated curved electrode zipping actuators with low pull in voltage. TRANSDUCERS 03, The 12th International Conference on Solid State Sensors, Actuators and Microsystems, Boston.

[54] M. Shikida, K. Sato, and T. Harada. (1995). Micromachined S-shaped actuator. IEEE Sixth International Symposium on Micro Machine and Human Science, 8:167-172.

[55] M. Yamaguchi, S. Kawamura, K. Minami, and M. Esashi. (1993). Distributed electrostatic micro actuator. IEEE Conference on Microelectromechanical Systems, FL, 18-23.

[56] R. Legtenberg, J. Gilbert, and S. D. Senturia. (1997). Electrostatic curved electrode actuators. Journal of Microelectromechanical Systems, 6:257-265.

[57]R. Jebens, W. Trimmer, and J. Walker. (1989). Microactuators for aligning optical fibers. Sensors and Actuators, 20:65-73.

[58] J. Branebjerg and P. Gravesen. (February 1992). A new electrostatic actuator providing improved stroke length and force. <u>IEEE Conference on Microelectromechanical Systems</u>, Travemunde, Germany, 6-11.

[59] V. K. Pamula, A. Jog, and R. B. Fair. Mechanical property measurement of thin-film gold using thermally actuated bimetallic cantilever beams. <u>Semiconductor Research Laboratory, Duke University.</u>

[60] M. T. Hou and R. Chen. (October 2002). Effect of width on the stress-induced bending of micromachined bilayer cantilevers. <u>Journal of Micromechanics and Microengineering</u>, 13:141-148.

[61] M. W. Judy, Y. Cho, R. T. Howe, and A. P. Pisano. (1991). Self-adjusting microactuators (SAMS). <u>Proc. IEEE MEMS (MEMS'91)</u>, 51-56.

[62] W. H. Chut, M. Mehreganyt, and R. L. Mullen. (February 1993). Analysis of tip deflection and force of a bimetallic cantilever microactuator. <u>Journal of Micromechanics and Microengineering</u>, 3:4-7.

[63] S. Chowdhury, M. Ahmadi, and W. C. Miller. (February 2005). A closed-form model for the pull-in voltage of electrostatically actuated cantilever Beam. <u>Journal of Micromechanics and Microengineering</u>, 15:756-763.

[64] www.matweb.com

[65] Q-A. Huang and N. K. S. Lee. (1999). Analysis and design of polysilicon thermal flexure actuator. <u>Journal of Micromechanics and Microengineering</u>, 9:64-70.

[66] D. Yan, A. Khajepour, and R. Mansour. (May 2004). Design and modeling of MEMS bidirectional vertical thermal actuator. <u>Journal of Micromechanics and Microengineering</u>, 14:841-850.

[67] Q-A. Huang and N. K. S. Lee. (February 1999). Analytical modeling and optimization for a laterally-driven polysilicon thermal actuator. <u>Microsystem Technologies</u>, 5(3):133-137.

BIOGRAPHICAL INFORMATION

Naresh Dhaubanjar received his BS degree in Science from the Amrit Science College, Kathmandu, Nepal in 1996. He received his Bachelor of Science in Electrical Engineering degree from the University of Texas at Arlington in May 2003. He received his Master of Science in Electrical Engineering degree from the University of Texas at Arlington in August 2006. His research interest includes Bio-MEMS, RF MEMS, RFIC and medical imaging.